Measurement of Ebullition Rates in a Mediterranean Climate Reservoir Using Hydroacoustic Measurements

By

KENDALL C. GALVEZ

THESIS

Submitted in partial satisfaction of the requirements for the degree of

MASTER OF SCIENCE

in

Civil and Environmental Engineering

in the

OFFICE OF GRADUATE STUDIES

of the

UNIVERSITY OF CALIFORNIA

DAVIS

Approved:

Alexander Forrest, Chair

Holly Oldroyd

Fábian Bombardelli

Committee in Charge

2024

ACKNOWLEDGMENTS

Thank you to my advisors, Dr. Alexander Forrest and Dr. Holly Oldroyd, who provided me with the amazing opportunity to pursue my Master's degree under their unwavering guidance and support. They both advocated for me and drove me to push the boundaries of what I thought was possible for myself. Thank you for sharing your knowledge with me. Thank you to Dr. Fábian Bombardelli for providing me with insight into the work I was doing and giving me helpful ideas. He was constantly encouraging me and was pushing me to explore more ideas.

Thank you to everyone in the Environmental Dynamics Lab at UC Davis. Each person in this lab has provided me with guidance in various ways that I am extremely grateful for. Jade Hinson helped motivate me and gave me feedback on figures and writing that elevated my thesis. Oscar Sepúlveda Steiner provided me with guidance and feedback on many aspects of this thesis, he truly expanded my view on scientific research that is invaluable. Drew Friedrichs helped me learn valuable coding skills that excelled my work for this thesis. Ruth Thirkill established a strong relationship with our Spanish collaborators and developed a guiding outline for this deployment, without her foundational work, it could not have been done.

Finally, thank you to our Spanish collaborators, Dr. Cintia Luz Ramón Casañas and Dr. Francisco Rueda at the University of Granada, Spain. Both hosted me and gave me comfort and guidance during my first time abroad. They made the experience unforgettable. They have also been guiding me and providing invaluable feedback and steps to progress this work. Despite the time difference, they have made it work and I am extremely grateful.

This work is dedicated to my grandparents: Christopher Robert Kluse, Edna Marie Kluse, Manuel Galvez, and Gloria Galvez.

To my grandparents who continuously taught me that nothing can replace hard work and kindness. Nothing great is made without hard work and the soul is not filled without kindness and giving back to those who need it most. They have fostered me into a strong, independent woman who can achieve anything. Thank you for everything and generations of valuable pillars of character.

ABSTRACT

Acoustic measurements have emerged as a promising method for monitoring methane fluxes (both diffusive and ebullitive) from reservoirs. With a current underestimation of methane generation from reservoirs and lakes, a reliable and accurate method to determine emission flux rates is necessary for expanding this area of study. The work described in this study used a BioSonics DT-X Extreme Echosounder in autonomous mode over a month-long period to develop a reliable technique for determining bubble sizes and frequency from a stationary platform in a Mediterranean climate reservoir in Granada, Spain. Traditionally used for fish detection, BioSonics Visual Aquatic single echo detection (SED) tracks can identify bubble plume tracks if properly configured, providing data on rising velocities and the linearity of detected paths. Data were recorded for 10 minutes, followed by a 10-minute break to conserve battery power over a month. By applying a relation between rising bubble velocity and bubble radius developed by Wüest et al. (1992) and a force balance for a single bubble rising through the water column, bubble volumes were determined from individual rising velocities. These results were analyzed with data collected by a different method (automatic bubble trap) on the same platform, confirming that the combined method produced comparable resolved bubble sizes. Volumes were then converted to ebullitive rates in milliliters per unit area per time. The ebullition rates derived from this method were compared with data from an SENECT ABT operating concurrently in the same area, revealing results of similar magnitude and trends. The findings demonstrate that this approach is a new method to determine valid ebullitive rates using stationary deployments that can similarly be applied to transects in future work as well as in other systems that see fit, i.e. lakes, rivers, and ocean work.

TABLE OF CONTENTS

TABLE OF FIGURES

NOMENCLATURE

C_D	Drag coefficient, dimensionless
C_m	Added mass coefficient, dimensionless, ≈ 0.5
D	Bubble diameter, m
g	Acceleration due to gravity, m s^{-2}
μ	Dynamic viscosity, N s m^{-2}
r	Bubble radius, m
R	Ratio of liquid density to particle density, ≈1
Re	Reynolds Number, Re = ρυD μ^{-1}, dimensionless
σ_{BS}	Backscattering cross-section, m^2
TS	Target strength, dB
ρ	Density, kg m^{-3}
υ	Velocity, m s^{-1}

1 INTRODUCTION

This thesis is a qualitative and quantitative study of methane (CH_4) ebullition rates in a Mediterranean climate reservoir in collaboration with the University of Granada, Spain. Methane is a potent greenhouse gas that drives climate change through its ability to trap heat creating warmer temperatures. Warmer temperatures can drive methane emissions from natural sources like reservoirs. This harmful feedback loop, specifically driven by reservoirs, has been underestimated. Methane emissions from reservoirs have not been widely quantified. This study employs hydroacoustics to develop an in-situ, non-invasive method for measuring methane bubble fluxes from reservoirs that builds from methods previously developed. Different from previous work, this method does not require specific instrument configurations to match the ones of this study. This makes the method accessible to users who may not have the same specifications for sampling.

Methane is classified as a key global greenhouse gas by the US EPA. A single methane molecule can store about 120 times more heat than a carbon dioxide (CO_2) molecule moment to moment, but decreases with time [2], [3]. CH_4 has a lifespan of up to 12 years in the atmosphere [2], [4]. CH_4 is grouped into three source categories by the National Oceanic & Atmospheric Administration (NOAA): natural and anthropogenic microbial, fossil, and pyrogenic with natural microbial sources including wetlands [5]. Natural microbial sources account for ~30% of methane sources globally [5]. CH_4 has been consistently increasing in atmospheric concentration since 1984 and is the second largest gas contributor to climate change after CO_2 due to its shorter lifespan than CO_2 [2], [4], [6]. Sequestration of CH_4 from the atmosphere is understudied and overlooked as most efforts for atmospheric greenhouse gas removal are channeled towards CO_2 sequestering

[7]. Reservoirs serve society through many functions such as drinking water, hydropower via dams, and recreation. The Intergovernmental Panel on Climate Change (IPCC) counters the US EPA and NASA by classifying reservoirs as anthropogenic and grey infrastructure due to their societal function, but classifies lakes as non-anthropogenic and blue infrastructure [8], [9]. The standard method to quantify the global contribution from reservoirs and lakes is by multiplying the global reservoir surface area by emission rates [10]. The problem with this method for quantification is that the datasets for emission rates are limited in location (relative to system and globally), seasonality, and time of day, therefore the current estimate is not necessarily representative of global emission rates. There is a clear need for more measurements of these gas fluxes to accurately correct the contribution from reservoirs. In-situ measurements of gas fluxes are increasing and are correcting the global estimates [10].

Methane is produced from reservoirs and lakes through a process called methanogenesis [11], [12]. Methanogenesis is the reduction of carbon (most commonly in the form of CO_2 and acetic acid) by microbes in the absence of oxygen [13], [14]. This process occurs at the bottom of the water column in the sediment and is dependent on temperature, water depth, and available organic carbon [12]. There are two main pathways for the release of methane into the atmosphere from reservoirs, diffusion and ebullition, and a third pathway via transport through aquatic plant roots [9], [11], [12], [15], [16]. The third pathway will not be discussed as it is negligible at the study sites detailed in this work. Methods employed to determine aquatic methane fluxes are commonly used for the quantification of diffusive fluxes, thus ebullition is often grouped with diffusive measurements [17].

Diffusion is the process of high concentrations of particles moving towards areas of lower concentration to reach equilibrium; in terms of methane, there is accumulation in the anoxic

sediment that slowly diffuses into the water which is then released into the atmosphere with the same process if it is not oxidized in the water column [18], [19]. The diffusive flux is typically measured via water surface or water column sensors and dissolved gas samples [9], [11], [20]. This study focuses on methodology to calculate ebullitive fluxes and so diffusion will not be included. Ebullition is the release of gas, via bubbles, formed within the sediments that can travel up toward the surface or dissolve along its pathway and varies heterogeneously temporally and spatially [16]. Lower fluxes typically represents diffusion, while high fluxes are associated with ebullition [20]. From CH_4 emissions data across 32 different reservoirs, ebullition dominated across 75% of the reservoirs accounting for more than 50% of total emissions at those reservoirs [9]. The ratio of diffusion to ebullition for each system is highly variable, which demonstrates the importance of separating collection methods for each pathway [17]. Reservoirs that are susceptible to high sediment loading and anoxic conditions typically produce more methane as these are ideal conditions for methanogenesis to occur [9], [11]. It was found that shallow reservoirs are more susceptible to these ideal conditions, as their water storage capacity reduces faster than larger reservoirs [11]. Ebullitive CH_4 was found to happen more frequently in depths shallower than 10 m across 32 different reservoirs [9].

Higher ebullitive fluxes seen in shallow water columns can be driven by a reduction in hydrostatic pressure at the sediment-water interface, which drives gas decompression in the sediment [21], [22]. Additionally, short-term water level fluctuations, generated by hydrodynamic processes that last seconds to hours, drive mechanical energy which can increase sediment transport and the release of methane trapped in sediments [23]. These hydrodynamic processes can include anthropogenic traffic, basin oscillations (e.g. seiche production), and surface waves driven by wind shear [23]. Temperature is another factor that correlates with methane release as seen in various

studies on a seasonal scale, where warmer temperatures correspond to higher emissions [9], [22]. On average, methane fluxes are 2.5 times greater in the daytime, but the driver on this diel scale is likely wind triggering ebullitive events and lower methane oxidation from elevated photosynthetic active radiation [24]. Stratified and mixing lakes were found to have a diel pattern with a peak between 12:00 and 15:00 [24].

Some methods to determine ebullitive fluxes from reservoirs are sediment analyses, air-water interface gas chambers or eddy covariance, bubble counters, and hydroacoustic in-situ measurements. Through sediment analysis, the volume of gas in the sediment and the gas composition can be determined, although this process is time sensitive and intensive [11], [12], [25]. Air-water interface gas chambers are also more involved with the user collecting gas samples from the chamber periodically (e.g. every 10 minutes) over the entire deployment period at one site. These chambers are typically used for diffusive flux measurement, but can indicate the presence of ebullition [9], [17], [20]. Bubble counters are convenient as they measure the change in volume of gas being released at the surface of the water, however, they only cover one location continuously (multiple traps are preferred for a better understanding of a system) [18]. Fewer traps can return poor spatial resolution of a reservoir's ebullitive flux rate. Hydroacoustic in-situ surveys have the potential to resolve a greater surface area of a reservoir in terms of ebullition via transects with the transducer [11], [12], [16], [22], [26], [27]. This method can also help determine where to set up gas chambers and bubble traps or take sediment samples since spatial variability can be established [20], [22], [25]. With this study, a method for determining ebullition rates with a hydroacoustic transducer is provided to contribute to current emission studies. This method has proven useful for studies with large datasets using a stationary BioSonics DT-X Extreme

Echosounder deployment and software (Visual Acquisition 6 and Visual Aquatic) and does not rely on specific instrument configurations (e.g. sampling frequencies).

1.1 HYDROACOUSTIC TECHNOLOGIES FOR IN-SITU MEASUREMENTS

Determining ebullition in reservoirs and lakes is often done with inverted funnels as a bubble trap to measure the released gas volume at the surface. However, hydroacoustics have proven to be another valid method for determining ebullition at the sediment instead of the surface through various studies [11], [12], [16], [22], [27], [28]. Not only does it provide high frequency and high resolution of results, it "has a huge potential for the noninvasive appraisal of spatial heterogeneity of bubble concentrations in the water column," [16]. However, it requires consistent monitoring to measure temporal changes in gas storage. The framework for this study was produced with all these hydroacoustic methods combined coupled with theoretical models further explored in Section 2.

1.1.1 Ostrovsky et al. Method

Ostrovsky et al. [16] used a BioSonics dual-beam echosounder at 120 kHz calibrated at a standard target strength with a threshold of -80 dB to quantify the ebullition rates in a lake. The echosounder was set to 10 pings per second (pps) and a pulse width of 0.2 ms. The methods from Ostrovsky et al. heavily influenced the methods for this study. The results from their study found that the acoustic backscattering of a bubble increases with bubble volume. An empirical equation equating the backscattering cross-section with bubble volumes was determined; however, this study uses a specific set of instrument settings that could impact the results, leading that equation invalid in this study. The shape of rising bubbles of different volumes was also investigated through direct optical measurements. The variability of bubble shapes of the same volume was successfully determined

through lab experiments. The shape of a rising bubble will affect the target strength received and can increase the variability in backscattering (σ_{BS}). Through their results, bubble equivalent radii (the square of the horizontal radii multiplied by the vertical radii) up to 0.4 mm were typically found to have spherical shapes, ellipsoidal up to 1.0 mm, and complex shapes larger than 1.0 mm radii. From the findings in their study, an empirical relationship between rising velocity and bubble volume was established for volumes between 0.005 mL and 20 mL. The rising velocities of contaminated bubbles – those found in uncontrolled environments like reservoirs – typically had radii ranging from 1 mm to 4 mm. Due to shape variability in this size range, the rising velocities cannot discern bubble volume with a high degree of certainty. The empirical relationship of rising velocities and bubble volumes matched the results of a laboratory experiment conducted by Haberman and Morton [29], but volumes smaller than 0.005 mL were not included in their study.

1.1.2 Maeck et al. Method

Maeck et al. [11] used a Simrad EY60 echosounder at 120 kHz to survey the Saar River, which flows through northeastern France and western Germany, and detect bubbles rising. The volumes of the bubbles detected were estimated by an empirical relationship following the Ostrovsky et al. [16] procedure. Intense ebullition was found to occur closer to the dam and had bubble radii ranging from 0.4 to 12.6 mm with an average of 2.8±1.2 mm. The fluxes varied spatially and temporally. At this site, ebullition was the dominate pathway for methane release into the atmosphere. Ebullitive fluxes showed a seasonal variation [29], [33], [34] with an average higher rate in warmer months (273 ± 131 mmol $m^{-2}d^{-1}$) and an average lower rate in the winter season (38 ± 73 mmol $m^{-2}d^{-1}$).

1.1.3 Martinez and Anderson Method

Martinez and Anderson [12] investigated ebullition gas fluxes in a shallow (average depth of 4.8 m), eutrophic lake (Lake Elsinore, CA) using BioSonics DT-X Echosounder at three frequencies 430 kHz, 201 kHz, and 38 kHz all at 5 pps. It was estimated that at 5 pps with a known depth, the average rising velocity for a bubble is 0.22 m s^{-1}. Across 7 sites, the shallowest site had the largest ebullition rates during two out of three sampling dates (the third sampling date in December 2010 had negligible rates across all sites in comparison to the other two dates). The rate of ebullition in the shallowest site during July 2011 was 96±2 mmol $m^{-2}d^{-1}$ compared to the deepest site's rate of ebullition in July 2011 of 13 ± 4 mmol $m^{-2}d^{-1}$. It was found that no significant detection of ebullition (<0.02 mmol $m^{-2}d^{-1}$) occurred across all sites in December 2010, significant ebullition occurred in July 2011 across all sites, and then dropped sharply (more than a 50% decrease on average) by September 2011. This supports the idea that seasonal variability influences the overall ebullitive flux. The ebullition gas fluxes at this study site were found to be a function of sediment types for gas storage, temperature, and seasons. It was also concluded that the dissolution probability of the bubbles is low since the lake is shallow with a short residence time. This study supports the notion that shallow reservoirs and lakes can be large contributors of methane to atmosphere via ebullition.

1.1.4 Shiba Method

Shiba [27] explored methane release mechanisms from lake sediments using BioSonics DT-X Echosounder at 201 kHz at 5 pps. This study was conducted at Lake Elsinore, CA, like Martinez and Anderson [12]. Shiba follows Ostrovsky et al. [16] and Martinez and Anderson [12] methods by using an average bubble size of 0.097 cm^3 and an average methane content of 85% with dissolution being negligible. With those assumptions, an empirical solution was developed to find

the diameters of single bubbles with their known target strengths. From the conducted study, the average rising velocity of the bubble released from lake sediments was 0.21±0.2 m s^{-1}. Sampling occurred in July, September 2014 and June 2015. Across four different sites and dates, the shallowest site (1.7 m depth) had the largest ebullition rates at 15,728 bubbles m^{-2} d^{-1} and the lowest rate at one of the deeper sites (5.8 m depth) at 2,253 bubbles m^{-2} d^{-1}. Shiba has a site at a similar depth to that at the Cubillas platform (3.7 m depth) and was sampled around the same time of year as this study (September 23rd, 2014). Lake Elsinore had an ebullition rate of 3,941 bubbles $m^{-2}d^{-1}$. It was found that there was no significant increase in ebullition from July to September 2014. Additionally, clusters of bubbles were seen spatially, meaning that multiple bubbles were released from specific locations in the sonar's footprint in short periods. Some of the locations had multiple bursts over time while others only had one burst.

1.1.5 Tušer et al. Method

Tušer et al. [22] collected ebullition data via acoustic surveying to find seasonal and spatial distributions in a reservoir. Using a Simrod EK60 at 120kHz, single echoes were detected and determined to be bubble tracks by movement patterns. Fish fail to move vertically in the same manner as a bubble. Similarly to Ostrovsky et al. [16] and Maeck et al. [11], an empirical equation was used to determine the volume of the bubbles released. It was found that ebullition does correlate with season, depth, and inflow data. Ebullitive fluxes increased with warmer temperatures but had the most significant emissions in the fall instead of July-August. This likely occurred due to the sediments reaching their annual maximum temperature and the bubbling areas expanding into deeper parts of the reservoir. It was also found that ebullition occurred more frequently in the shallower depths near the river inflow, suggesting that there is less hydrostatic pressure on the sediment and higher organic matter distributions.

1.2 OBJECTIVES OF STUDY

Because previous studies rely on empirical solutions to determine bubble volumes, developing a method that can find bubble volumes regardless of the echosounder's frequency is crucial for advancing this research and making it more accessible to others. The objective of this study is to develop a method to quantify the bubble release rates in one area of the reservoir, a platform at 4 m depth) to gain a better understanding of the system's ebullition rates using hydroacoustic measurements. The study works with datasets collected via a BioSonics DT-X Extreme Echosounder. The release of methane via ebullition was evaluated in one area via an autonomous stationary deployment of the BioSonics DT-X Extreme Echosounder for the duration of a month. BioSonics DT-X Extreme Echosounder records returning target strength [dB] in the water column to produce a single echo detection (SED) track determined to be a rising bubble. Each rising bubble had a recorded rising velocity. Rates of ebullition gas fluxes were determined from recorded rising velocities using a force balance of a single spherical bubble and a sizing distribution developed by Wüest et al. [1] to determine which approach produces results comparable to measured automatic bubble trap data. This study focuses on ebullitive fluxes and does not investigate concurrent diffusive flux measurements. The proposed method for quantifying ebullition starts with understanding the physics of bubbles in water and applying that knowledge to large sets of data efficiently. Combining this method with meteorological data and previous studies can provide insights into a system in a changing climate. Applying this method to transects is part of future work for this research.

Early experiments exploring bubble velocities and drag forces will be discussed as a foundation for implementing a force balance into this study. Different findings of drag coefficients and bubble force balances will also be explored as guidance for this study. Previously found relationships

between rising velocities and bubble radii combined with bubble force balances will be used as a method to find ebullition from hydroacoustic data that records rising velocities. To validate the method's results, the data will be compared to found bubble trap data that will be coupled with meteorological and the reservoir's data.

2 THEORY

2.1 FORCE BALANCE OF A RISING BUBBLE

This study aims to quantify the amount of methane released via ebullition. BioSonics DT-X Extreme Echosounder can determine individual tracks with relevant parameters. The known parameters of this study are rising velocities of the bubbles, time of release, and location of release. A force balance on a single bubble is an appropriate approach with the known parameters to determine the volume of gas released into the atmosphere. Detailed methods for finding relevant parameters using BioSonics software and technology can be found in the section.

2.1.1 Drag Coefficients of Bubbles

Various datasets were considered to determine what drag coefficient, C_D, to use, to find the most accurate value for this study. According to a study conducted in 1953 by Haberman et al. [30], the drag coefficient of a spherical cap bubble rising in a liquid has a value of 2.6 regardless of size and is in agreement with earlier studies conducted by Rosenburg and Basin in 1950 [30], [31]. Rosenberg and Basin's method for determining the drag coefficient was done experimentally with a tank large enough to avoid wall effects in 19.4°C water [31]. Small bubbles were released via nozzles of varying sizes and larger bubbles were created by collecting smaller bubbles in a cup which were then rotated to release them [31]. Using film cameras, motion pictures of the rising bubbles were created and scaled to determine the rising speed and shape of the bubbles. Additional experimental data were also included in the study to see how it aligned to the results found. These additional datasets added significant scatter that clustered around a drag coefficient of 2.6 for Re > 400. The addition of more data showed the variability in the results. Within this variability, there are values that range from ~0.13 through 2.6, particularly for Re > 350 and Re < 2000. However,

a C_D of 2.6 was deemed valid for spherical cap bubbles due to the geometric similarities between each bubble. A major disadvantage to using this found value is that the value was found in a laboratory setting, which is extremely idealistic and controlled as well as the variability in the results. It assumes that the shape of each bubble is strictly a spherical cap. In open water, having spherical cap bubbles with each release from the sediment is not likely to occur due fractures in the sediment releasing the bubble versus a controlled circular nozzle.

Aybers and Tapucu [32] conducted various laboratory experiments and focused on determining terminal velocities and drag coefficients for varying diameters and motions. Average velocities for different depths were recorded. A C_D equation for rectilinear motion bubbles (Re < 565) and is derived from buoyancy equating to drag:

$$C_D = \frac{4}{3}\frac{gD}{v^2} \tag{1}$$

where g refers to acceleration due to gravity, D refers to the equivalent bubble diameter, and v refers to the bubble's average rising velocity. Eq. 1 is assuming the path of the bubble is strictly in the z-direction which only has drag and buoyancy involved, and is expanded on further to include the path's angle relative to the release point. Due to unknowns in this study, Eq. 1 is used without the path's angle included.

By Karamanev and Nikolov, a valid constant C_D value is 0.95 [33]. The experiment consisted of a cylindrical tank filled with tap water at 23°C. Wall effects were considered negligible here. Bubble velocities were measured from exposure time from a camera with various exposure times (1.00, 0.50 and 0.25 seconds) and diameters were determined using a micrometer. The drag coefficients were determined using an equation similar to Eq. 1. Karamanev and Nikolov [33] added density terms to account for the different densities of the particle and liquid.

$$C_D = \frac{4gD(\rho_l - \rho_p)}{3\rho_l v_t^2} \quad (2)$$

where ρ_l refers to the density of the liquid, ρ_p refers to the density of the particle, and v_t is the terminal rising velocity. It was observed that particles in the terminal Reynolds Number, Re, range >130 were constant and equal to 0.95±11% [33]. Following Karamanev and Nikolov [33], the estimation of 0.95 is independent of particle densities below 300 kg/m^3.

Since the drag coefficient's variability was found to be significant through preliminary calculations (contrary to Rosenburg and Basin [31] and Karamanev and Nikolov [33]), it is essential to account for it as accurately as possible. Yan et al. [34] explored various drag coefficient equations to determine which results in values that best match experimental values. Their approach investigated the drag coefficient of a single rising bubble in deionized water. Yan et al. investigated various C_D equations related to Re:

$$C_D = \frac{24(1 + 0.15Re^{0.687})}{Re}, Re \leq 1000 \quad (3.1)$$

$$C_D = 0.44, Re > 1000 \quad (3.2)$$

Equations 3.1 and 3.2 were determined by Schiller and Naumann in 1935, and it is widely accepted as an estimate. Equations 3.1 and 3.2 were found to have an overestimation or underestimation when compared to experimental data found from Eq. 1 using an averaged terminal velocity. This over and underestimation occurred due to bubble deformation being ignored. It was found that drag coefficient equations that account for this deformation through Eötvös number (Eo), a ratio between gravitational forces to capillary forces, and Weber number, a ratio between the rising velocity, fluid density, characteristic length to surface tension, have better agreement with experimental findings [35], [36].

2.1.2 Force Balances with Different Models

A force balance equation for bubble rise was developed by Manica et al. [37] that uses the following force balance for the motion of a point particle [37]:

$$\sum F = F_A + F_B + F_D + F_F = ma \approx 0 \tag{4}$$

where F_A is the added mass force from the bubble, F_B is the buoyancy force, F_D is the drag force, and F_F is "the film force due to the lubrication pressure build up in the film between the deformed bubble and the surface," [37]. The mass of the bubble is typically negligible, but the acceleration creates an inertial effect that needs to be accounted for [37].

Each term in Eq. 4 is defined by Manica et al. [37] as follows:

$$F_B = -\rho g \frac{4}{3}\pi r^3 \tag{4.1}$$

$$F_D = C_D Re \frac{\pi}{4}\mu r v \tag{4.2}$$

$$F_A = \frac{4}{3}\pi r^3 \rho C_m \frac{dv}{dt} \tag{4.3}$$

$$F_F = \left(\int_0^\infty 2\pi r p \; dr\right)\boldsymbol{k} \tag{4.4}$$

where r is radius of the bubble, μ is the dynamic viscosity, C_m is an added mass coefficient, and p is pressure in the film calculated from film drainage Stokes-Reynolds equation. For this model, an assumption of a steady state is necessary to solve the entire force balance. C_m has a constant value of 0.5. Manica et al. [37] use Eq. 3.1 and 3.2 for the C_D term.

2.2 BUBBLE PLUME MODELING BY WÜEST ET AL. 1992

In pursuit of creating a bubble plume model, Wüest et al. [1] needed to find an approximation for bubble slip velocity from known bubble radii. Using Haberman and Morton [29] data of bubbles

rising in tap water and distilled water, an approximation for slip velocities was found for radii ranging from 0.1 mm to 40 mm, see Appendix Figure A- 1. The following set of equations is the approximation solving for radius [m] instead of velocities [1]:

$$r = \sqrt[1.357]{\frac{\nu}{4474}} \qquad \upsilon < 0.23 \text{ m s}^{-1} \qquad (5.1)$$

$$7.0*10^{-4} < r < 5.1*10^{-3} \qquad \upsilon = 0.23 \text{ m s}^{-1} \qquad (5.2)$$

$$r = \sqrt[0.547]{\frac{\nu}{4.202}} \qquad \upsilon > 0.23 \text{ m s}^{-1} \qquad (5.3)$$

For Eq. 5.2, there was found to be a plateau that occurred at a slip velocity of 0.23 m s^{-1}. For this range of radii, it is assumed that there is an equal distribution. This plateau occurs due to the changing shape of the rising bubble [38]. The velocity of the rising bubble increases with its size until it reaches a magnitude of approximately 0.23 m s^{-1}, it then flattens out to a spherical cap shape which increases the friction experienced by the bubble [1], [30], [38]. Once it reaches a large enough aspect ratio, which is the larger radius to the shorter radius of the bubble, size dominates allowing for the velocity to proportionally increase with the radius [38].

3 METHODOLOGY

3.1 STUDY SITE

Cubillas Reservoir is in Granada, Andalusia, Spain. The area has a Mediterranean-temperate climate in the Northern Hemisphere. There are few precipitation events in the region and the summer months of June to September are generally hot with an average high of 33°C, taken from nearby meteorological stations. The reservoir falls in the path of Río Cubillas (Cubillas River) which has an origin in Sierra Arana, a mountain unit in Granada. Cubillas Reservoir is a shallow reservoir that has a maximum depth of approximately 6 meters near the forebay of the dam in the summer months (CTD Casts). The primary uses of the reservoir and dam are irrigation, water supply, recreation, and electricity [39].

During deployment, Cubillas Reservoir was consistently, visually active in terms of ebullition. While conducting various surveys on the reservoir, bubbles sitting on the surface in the early morning from the nighttime undisturbed by the afternoon winds and bubble plumes were consistently observed. Along with visual confirmation of ebullition, the sediment samples had the scent of hydrogen sulfide, indicating the presence of decaying organic matter, a sign of methanogenesis [40].

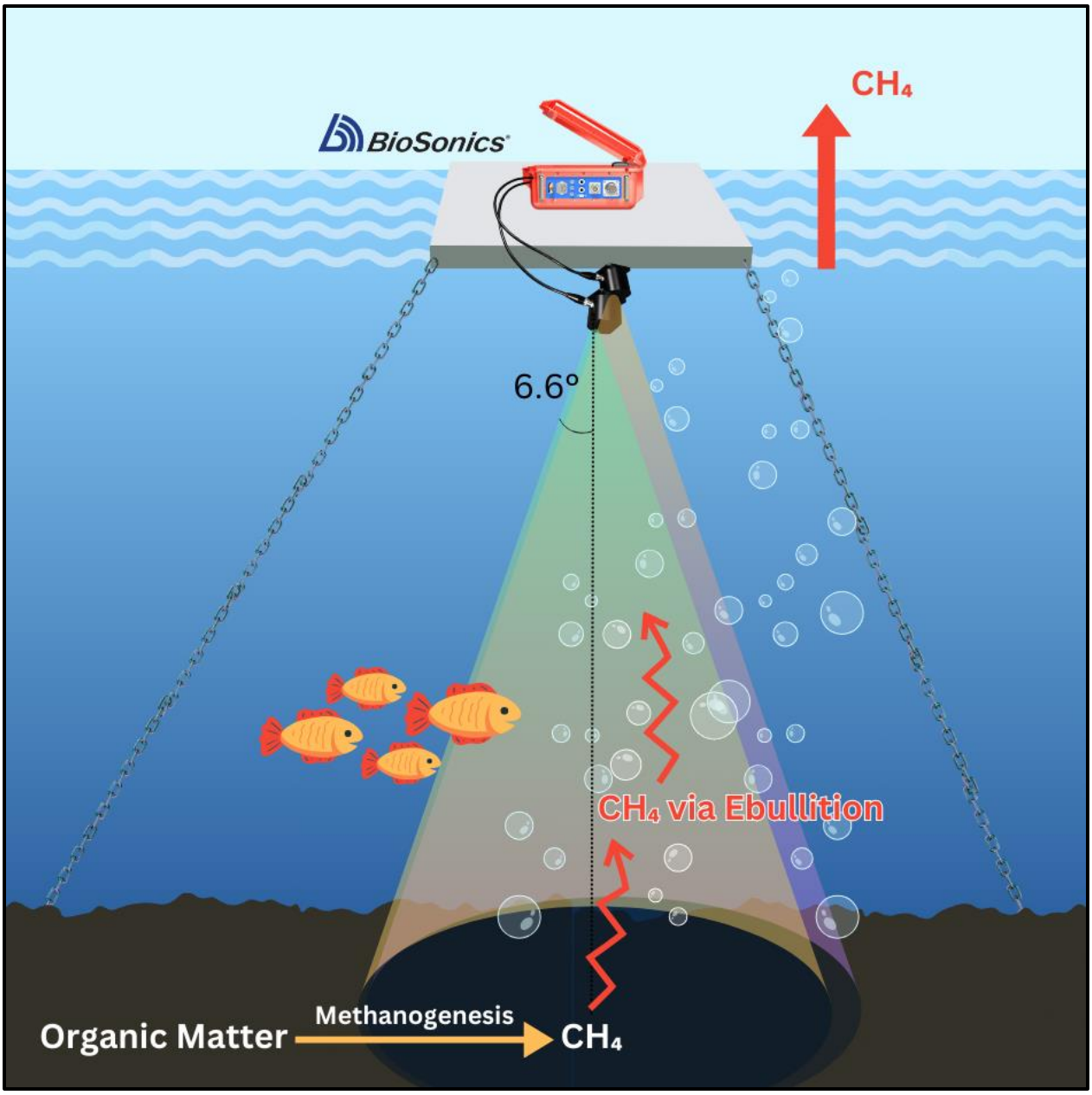

Figure 1. Cubillas Reservoir platform setup diagram. BioSonics DT-X Extreme Echosounder dual-beam configuration off the stationary platform.

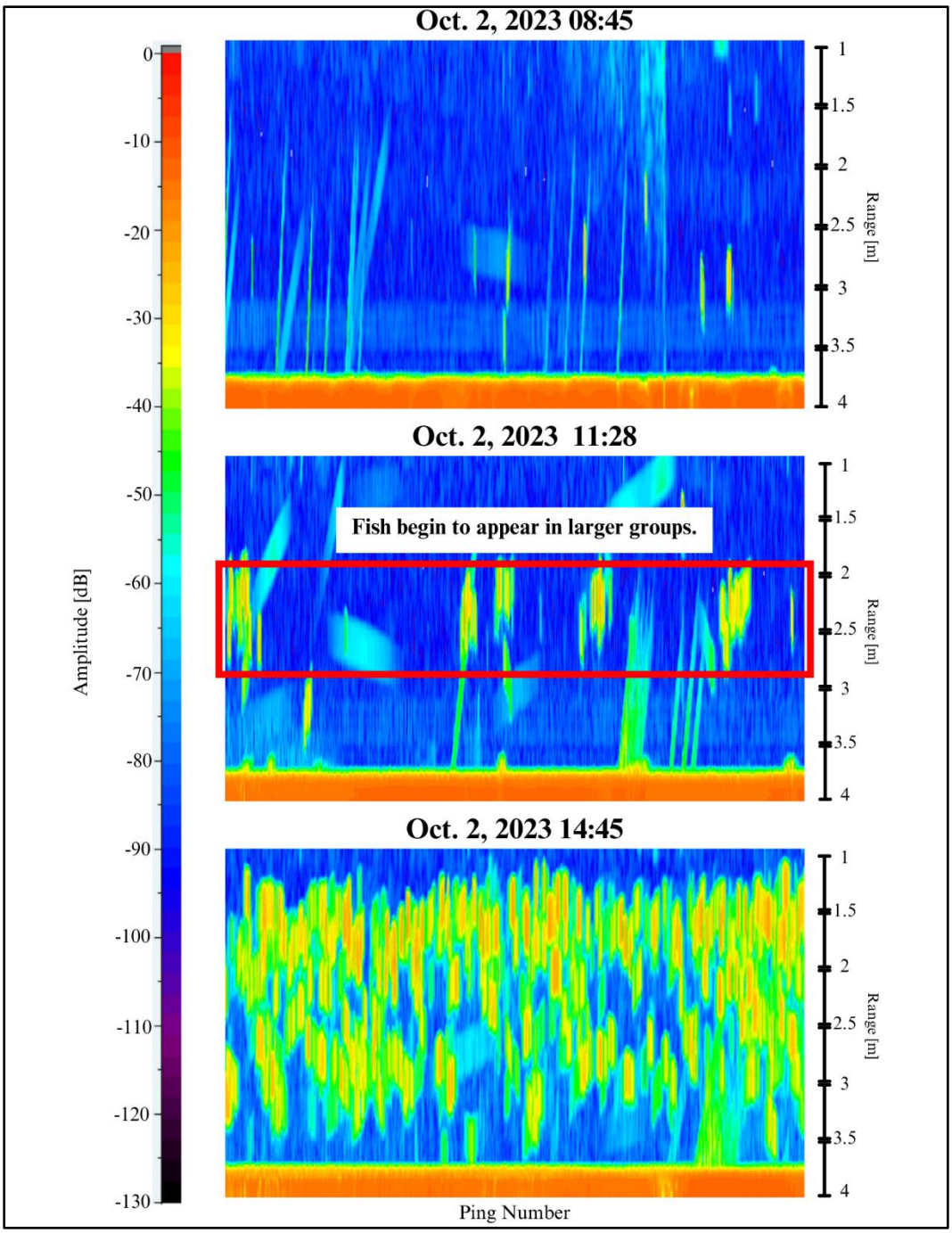

Figure 2. Echogram from the morning of October 2nd, 2023, shows little interference from schools of fish. The range is 1 m below the surface to approximately 3.8 m along the y-axis with pings in time (5 pps) along the x-axis. As the day progresses, more fish appear, blocking the diagonal streak lines which are bubbles. Times are in CEST.

3.1.1 The Platform

For the deployment of the BioSonics DT-X Extreme Echosounder, a stationary platform on the reservoir was used. The platform is in the northern section of the reservoir (37°16'41"N 3°40'19"W). The depth was approximately 3.8 meters at the time of data collection. The Echosounder was deployed off the edge of the platform and anchored on the sides to keep the signal pointing downward at a 90° angle (see Figure 1). In the event of strong winds or someone stepping onto the platform, the signal can detect different depths for the bottom, but can still detect SED tracks. A series of marine batteries were set up to solar panels always feeding the Echosounder a minimum voltage of 12 VDC. The BioSonics DT-X Extreme Echosounder will automatically shut off if the receiving voltage drops below 11 VDC [41].

It was observed from the implementation of this platform for various data collections, fish have adopted the area as a source of refuge from the sun. During the autonomous deployment, fish were observed in the data images in the late afternoon hours but were scarcely detected in the nighttime and early morning (Figure 2). This was found by observing the images received by the Echosounder. Visual Acquisition 6 and Visual Aquatic produce images called echograms. These images show a change in target strength received by the transducer heads, which can be deduced to bubbles or fish in the water column. Figure 2 shows echograms from a portion of the dataset, and the schools of fish are shown to appear in larger numbers as the day goes on.

3.2 IN-SITU MEASUREMENT

The deployment of BioSonics DT-X Extreme Echosounder over a month, from September 26th to October 26th, 2023, produced a dataset for our ebullition gas flux rates. During the one month, the

Echosounder was autonomously deployed to record data in 10-minute off/10-minute on intervals. This period produced 76 data time-blocks for each day.

The Echosounder was sampling at 5 pings s^{-1} at a frequency of 199 kHz. For BioSonics DT-X Extreme at a frequency of 199 kHz, the beamwidth in degrees is 6.6° x 6.6°. Using the depth of the water column and the angle of the beamwidth, the circular footprint of the transducer at the sediment has a 0.87-meter diameter. The volume of water swept by the transducer is approximately 0.769 cubic meters at 3.8 meters of water. The data were continuously recorded starting on September 28th, 2023, and ending on October 27th, 2023. The echograms were analyzed via Visual Aquatic, a BioSonics software. Single echo detection (SED) tracking was analyzed for the first meter above the sediment to minimize fish detection and to ensure the bubble was released from the sediment directly into the transducer's footprint.

The target strength (TS) for bubbles at the sampling frequency -199 kHz was found to be around -45 dB, where water was around -90 dB, and sediment at around -15 dB (Figure 2). The analyses for the echograms were set to have a threshold of -80 dB to track bubbles that may be faint in the return signal from being directly under fish or towards the outer edge of the footprint, which is in correspondence with Ostrovsky et al. lab experiments [16]. It was found in the manual analysis of the echograms that fish disrupt the return signal if they are directly underneath the transducer heads. At an acoustic frequency of 200 kHz, it was found that fish have an average TS of -30 dB to -40 dB [42]. If the analyses ran only accounted for target strength values, many fish would be wrongfully accounted as released bubbles. In the following section, configurations for analyzing the recorded echograms are listed. In addition, the echo level threshold for determining bubble tracks using Visual Aquatic would need to be tested to make sure its detecting bubbles in SED tracking if sampling at a different frequency. For example, Ostrovsky et al. [16] sampled at a

frequency of -120 kHz and a ping rate of 10 pings s^{-1}, so the -80 dB echo level threshold was initially tried as a starting point and was found to work for the collected echograms in this study.

3.3 VISUAL AQUATIC AND MATLAB DATA PROCESSING

SED tracking in Visual Aquatic produces CSV files that contain data for velocities in the x, y, and z directions, mean echo TS, linearity of the path in all directions, and other variables. In Visual Aquatic, the user uploads recorded .dtx or .rtp files into one dataset that can be analyzed as its files or as a group. The following configurations were made to the dataset analysis parameters to fit the site specifics and literature findings:

- Echo Detection Start Range: 3 m
- Echo Detection End Range: 4 m
- Echo Level Threshold: -80 dB
- Min Echo Length: 0.75 times pulse length
- Max Echo Length: 10 times pulse length
- Track Detection Start Range: 3 m
- Track Detection End Range: 4 m
- Tracking Window: 0.2 m
- Min Consecutive Echoes To Start Track: 3
- Min Additional Echoes To Accept Track: 0
- Max Ping Gap: 2
- Max Pings to Accept Track: 100

All other analysis parameters were at default settings. It is important to note that depth of the reservoir is a large factor in deciding ranges. The SED track was the only exported CSV files with

all columns in the “Track Listing” section selected. To run the initial MATLAB code for processing, these are the only CSV files needed. The CSV file exported has 79 columns and varying number of rows based on how many SED tracks were reported in that specific transducer file.

To ensure that the tracks were bubbles, two conditions had to be met: the rising velocity is $+0.21\pm0.09$ m s^{-1} and the linearity of the track is $+0.8\pm0.18$ found from a set of recorded echograms [12], [16], [27]. Creating a for-loop in MATLAB, the imported .csv files from Visual Aquatic were processed to determine if each track fit the two conditions. If the track did not meet both, it was discarded. Manual edits in Visual Aquatic were also made to discard any stray fish recorded. This was done at the data analyst’s discretion. For guidance, fish recorded in the echograms have horizontal movements with gradual changes in their rising slope, if any. In contrast, bubbles rise in a steep diagonal line leaning to the right (refer to Figure 2) [22]. Noisier tracks were unedited and left to only the two conditions in MATLAB to determine if they were a bubble or fish. To add a level of confidence, the SED tracks for bubbles were manually counted for a single random file and compared to the results processed through the MATLAB code for multiple files. After this processing, if a track is registered, it is assumed to be a bubble event.

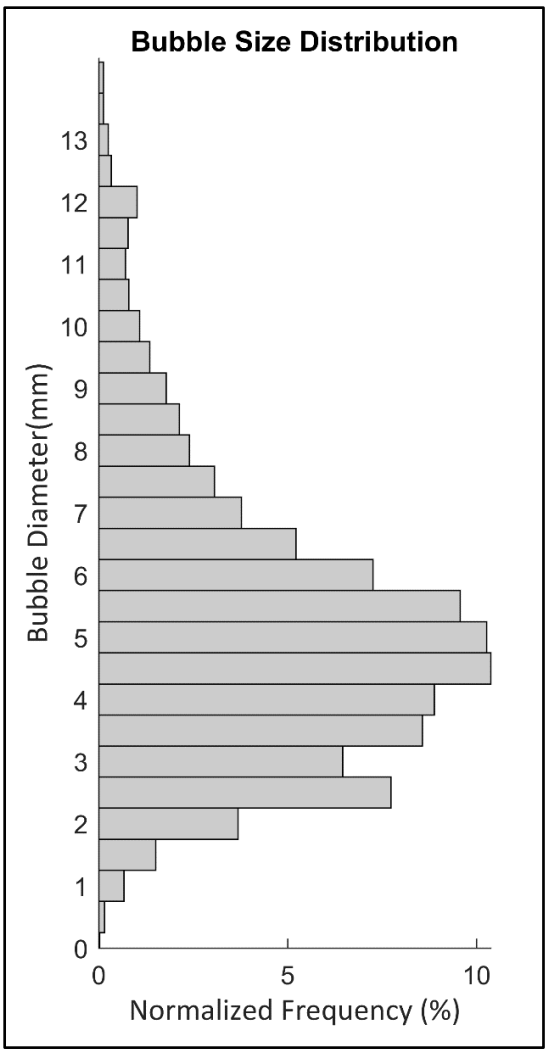

Figure 3. Bubble size distribution from July 2022 to November 2022. Note that there is a gap from August to October 2022. Collection via SENECT Automatic Bubble Trap counter. Provided by the University of Granada by Dr. Cintia Luz Ramón Casañas.

After processing all the datasets, determining the sizes of bubbles was conducted via MATLAB using Manica et al. force balance method [37], a developed iterative method, and the velocity-radius relationship from Wüest et al. [1]. As a point of reference, previously collected data from Cubillas Reservoir were used to guide the findings from each method. Figure 3 is a bubble size distribution found from a deployment during July 2022 to November 2022 using a SENECT Automatic Bubble Trap counter. There is a gap in the collected data from August to October 2022, meaning that the data only has July and November 2022 data. There is a wide range of diameters

from 0.17 mm to 14.3 mm with a peak normalized frequency at around 4.5 mm. Using Manica et al. method [37] (Eq. 3.1, 3.2, 4.1, and 4.2) as the first method, the diameters of single bubbles were resolved with the known velocities from Visual Aquatic SED tracking. The Manica et al. method [37] has a velocity derivative in Eq. 4.3 and was not included since it was undetermined for this system as there are over 21,000 individually recorded velocities. The force due to the film, Eq. 4.4, was also not included due to the pressure in each bubble's film being unresolved. From these two terms being removed, the Manica et al. method [37] did not produce bubble sizes within the expected diameter range (see Figure 3) and thus was discarded as a valid method for this study.

Newton's Second Law provides a force balance on a single bubble assuming steady state,

$$F_{buoyancy} = F_{drag} \tag{6}$$

which can be described as the following:

$$\frac{\pi}{6} D^3 \rho R g = \frac{1}{2} \rho C_D v_{bubble}^2 \frac{\pi}{4} D^2 \tag{6.1}$$

$$D = \frac{3 C_D v_{bubble}^2}{4g} \tag{6.2}$$

where *R* is the ratio between the difference of the densities of the fluid and the gas to the density of the fluid. Since water has a much higher density (~998 kg m^{-3}) than the gas in the bubble (~0.657 kg m^{-3}), *R* = 1. Equation 6.1 can be solved for diameter which results in Eq. 6.2. Initially, Eq. 6.2 was used with a constant drag coefficient determined from literature (refer to Section 2.1.1). It was found that using a constant drag coefficient did not provide diameters within the expected range (refer to Figure 3). To determine a more accurate expression for varying drag coefficients, Eq. 3.1 and 3.2 were used.

The Wüest et al. approximation set of equations [1] (Eq. 5.1, 5.2, 5.3) were programmed to solve for the radii outside the range in Eq. 5.2 with known velocities first. Eq. 5.2 has a large range of bubble sizes for rising velocities of 0.23 m s^{-1}. Initially, a uniform distribution is used in this radii range to resolve any bubble with rising velocities of 0.23 m s^{-1}. Solving for this range of radii at this rising velocity can also be done by using Eq. 3.1, 3.2 and 6.2 in an iterative method in MATLAB (See Appendix for code example). This is referred to as the iterative force balance method later. The code iterates through different diameters to find the best approximation. With an initial diameter guess, the code finds the Re with the bubble's velocity and initial diameter guess. The C_D is then updated based off the found Re. Using the new C_D value, Eq. 6.2 is used to find a new diameter. The initial and updated diameter are then compared to find an error less than or equal to 0.000001. Initial diameter guess (variable d0) was chosen because of its frequency in Figure 3 and gave results that showed high promise (refer to Section 4.2). The variable dum3 refers to the array of recorded velocities that equate to 0.23 m s^{-1} as seen in Eq. 5.2. From found sizes, volumes of the bubbles were found and calculated per unit area per unit time to find ebullitive rates over the entire deployment.

4 RESULTS

Over the entirety of the month for data collection, October 4th and 5th were the only dates that had technical issues with the collection from the BioSonics Echosounder. For those dates, the afternoon data was not collected, which will be visualized as gaps in the data. To validate the acoustic method for estimating ebullition rates, an Automatic Bubble Trap (ABT), produced by SENECT, was deployed during the same period. There were technical issues with the ABT for much of October and is visualized in the comparison plots.

4.1 METEOROLOGICAL AND RESERVOIR DATA

Cubillas Reservoir is in a Mediterranean climate which has hot summers and warm autumns gradually cooling into the winter months. Air temperature and wind speed were recorded during the deployment off the platform. Figure 4 shows a consistent diel pattern, with a gradual peak to the afternoon at 15:00 CEST, for both the air temperature and wind speed. However, October 14th shows a change in air temperature range and consistently cools as the month progresses. Wind speeds had a daily minimum at 03:00 or 09:00 CEST, with 09:00 being more frequent. After the minimum wind speed was reached, there are relatively sharp increases in speed peaking at 15:00 CEST. Wind speeds dramatically increase with large peaks at 15:00 CEST for 3 different days (October 17th, 19th and 22nd). Water level fluctuations occurred during the sampling period due to precipitation and outflow regulation via dam as seen in Figure 5. The water levels were recorded as meters above sea level and show a gradual decrease during the end of September corresponding to continuous release via the dam. During a relatively large precipitation event during the later hours of October 19th, the water level increases and eventually peaks to 636.1 m above sea level at the end of the sampling period, which is about a 0.02 m increase from the start date.

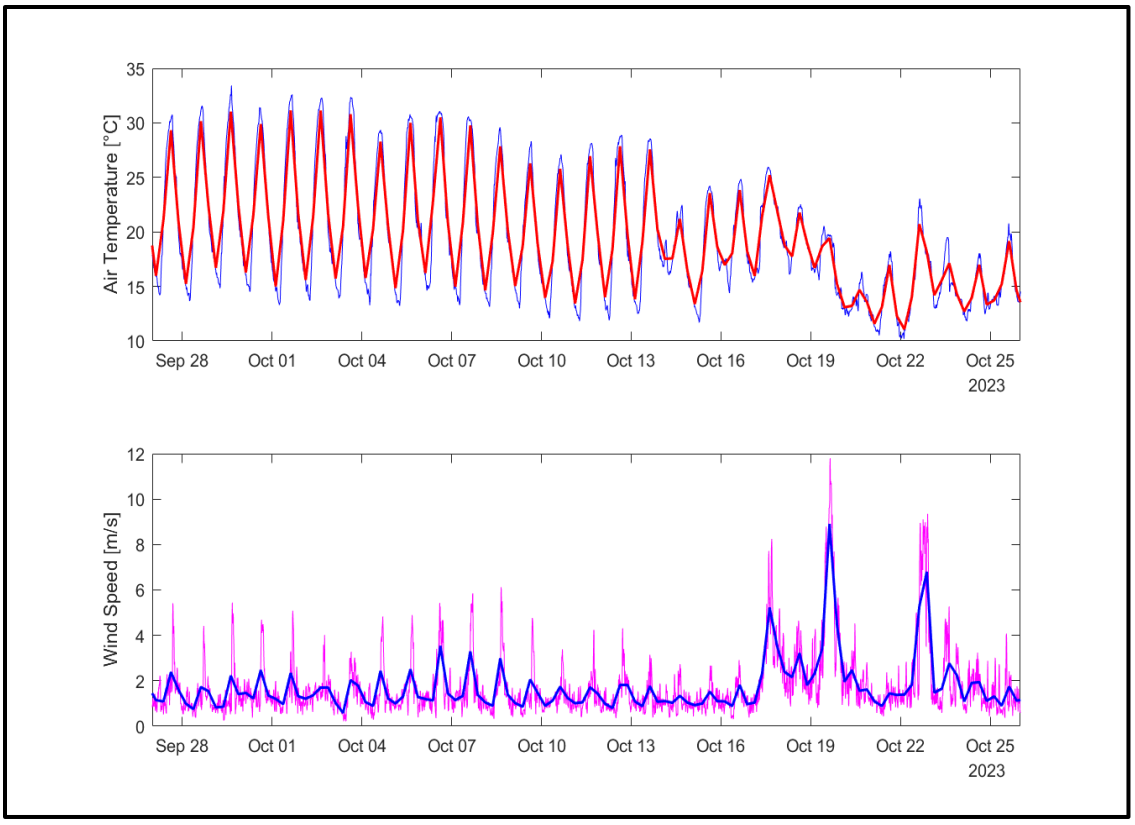

Figure 4. Top) Air temperature in degrees Celsius from September 27th, 2023 to October 26th, 2023. The red line represents the binned average for every 6 hours. Bottom) Wind speed in meters/second was recorded for the same period. The dark blue line represents the binned average for every six hours.

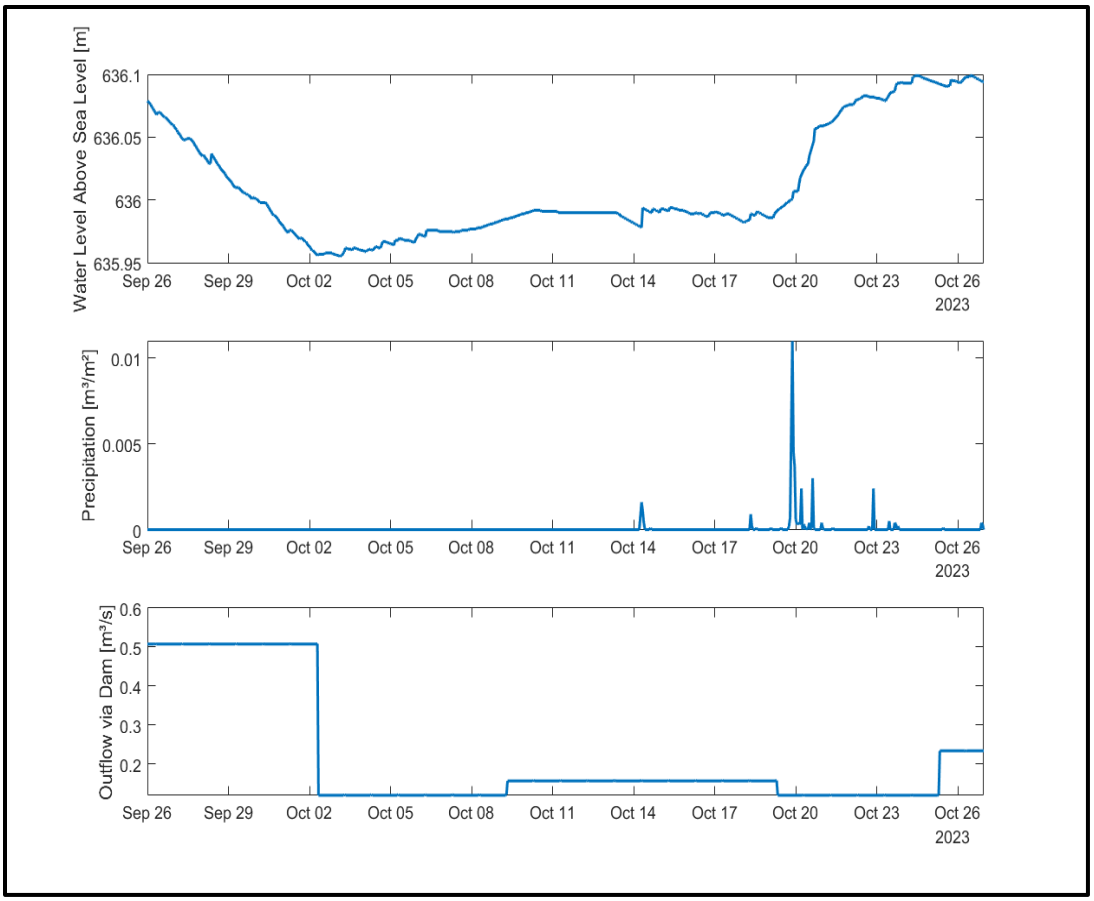

Figure 5. Top) Cubillas Reservoir water level fluctuations from September 26th, 2023 to October 26th, 2023. Middle) Precipitation events. Bottom) Outflow events via dam release.

Figure 6 is a calculated heat budget using the Livingstone and Imboden heat balance method with the collected meteorological data on the platform [43]. Peaks in the heat flux occur at the peak of short wave radiation in the afternoon, with heat loss during the nighttime due to no incoming shortwave radiation. The daily average in Figure 6 shows a slight decrease moving through the month and has lower values during days with precipitation. This is expected for this time of year as the cooler months (typically November-January in the northern hemisphere) are approaching and the incoming shortwave radiation is decreasing [43], [44].

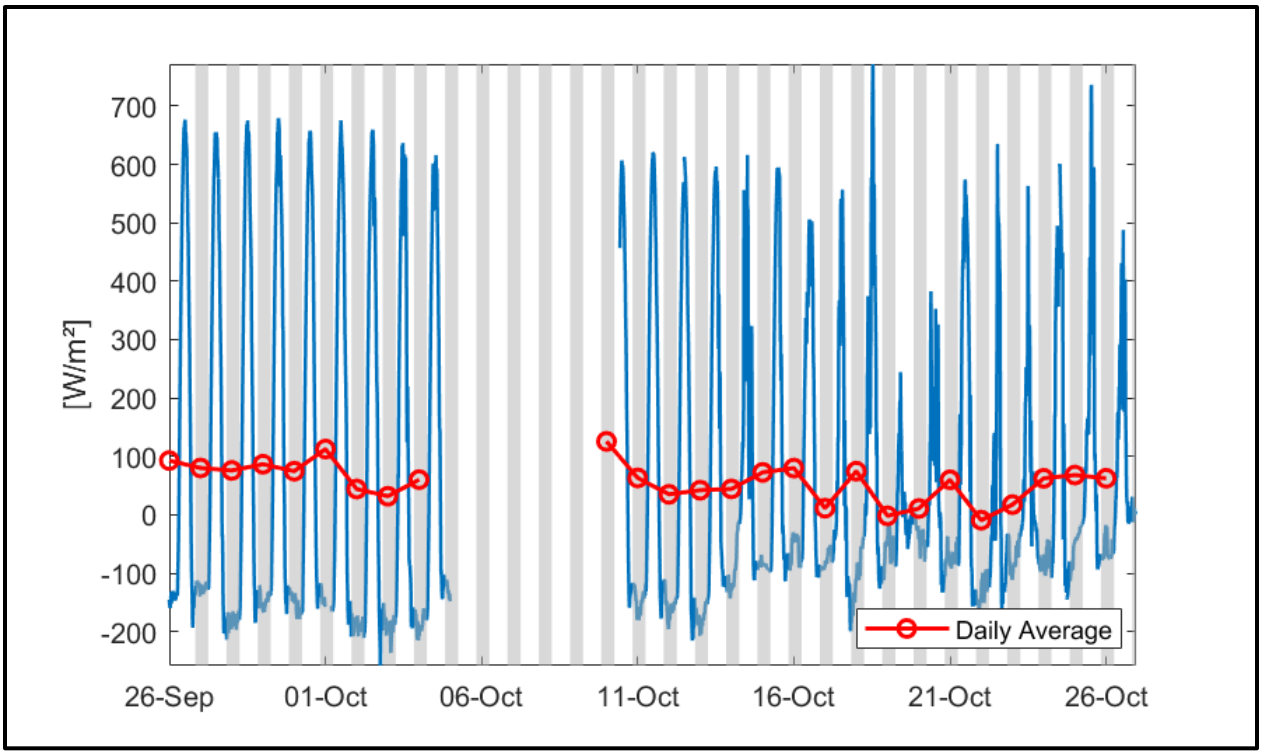

Figure 6. Heat Budget for Cubillas Reservoir using Livingstone and Imboden heat balance method from September 26th through October 26th, 2023 [43]. Grey shaded region represents the night hours. Gap in data occurred from missing thermistor chain data at the platform.

4.2 DISTRIBUTIONS

The recorded velocities extracted from BioSonics Visual Aquatic SED Tracking for the entire deployment ranged from 0.12 m s^{-1} to 0.3 m s^{-1}. Figure 7 has a slight left skew favoring lower rising velocities with the peak in the bin range 0.225 to 0.23 m s^{-1}. The arithmetic mean for the recorded rising velocities is 0.2167 m s^{-1}.

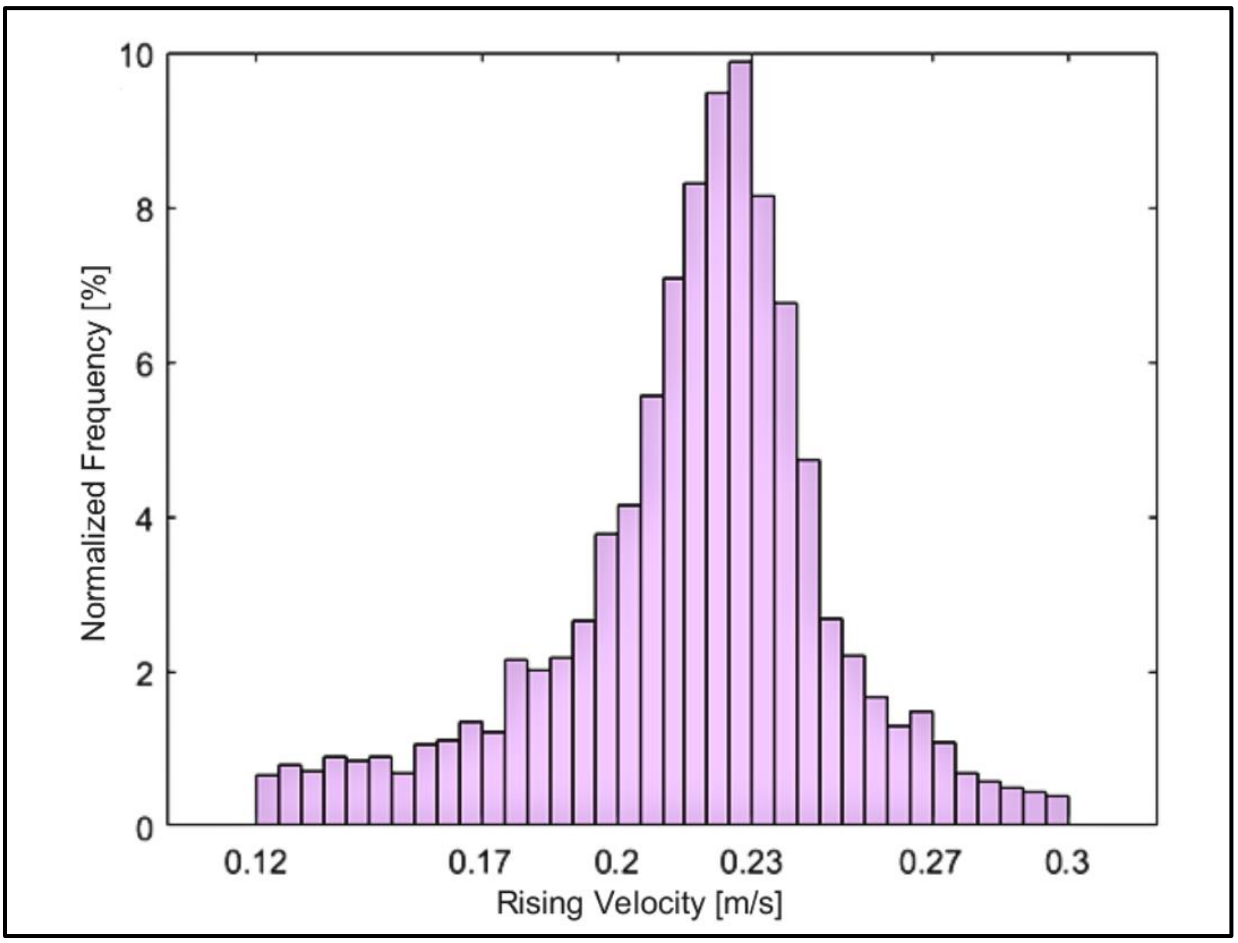

Figure 7. Rising velocities recorded by BioSonics Visual Aquatic SED Tracking during the entire deployment in 2023 binned into normalized frequencies.

Using the recorded velocities from the SED tracks in Figure 7, bubble sizes were calculated with the method in Section 3.3. Figure 3 is a reference point for the found size distributions using the hydroacoustic methods. As a reminder, Figure 3 has a normalized frequency peak at 4.5 mm with a right-skewed distribution. Data from Figure 3 is presented directly in Figure 8a and Figure 8b as the purple histograms to show how the methods compare. The dataset has a range of 0.17 mm to 14.3 mm. Using Wüest et al. approximations [1] (Eqs. 5.1, 5.2, and 5.3), the diameters of the rising bubbles were found from recorded velocities. Figure 8a shows the bubble size distributions for both the Wüest et al. [1] method and the iterative force balance method. Initially, the two methods

were used separately to obtain two sets of diameters for each recorded velocity. In Figure 8a, diameters found using the Wüest et al. method [1] showed a high peak in the 0.7 to 1.47 mm bin, with around 35% of the results falling there. There is a uniform distribution in the radii range corresponding with known velocities at 0.23 m s^{-1} from Eq. 5.2. At approximately 10 mm, there is a new peak with a right-skew for the remaining data. The iterative force balance method has a much narrower range for diameters which ranges from 2 to 8 mm. The distribution is more symmetric than the Wüest et al. approximation [1]. The majority for both methods are within the expected range of 0.17 mm to 14.3 mm from Figure 3 with some diameters reaching up to 16 mm. Figure 8b combines the theoretical Wüest et al. approximation [1] with the iterative force balance method solving for the range of radius (equivalent diameters were found and used for the histograms) in Eq. 5.2, as explained in Section 3.3. This created a distribution of diameters in the range from Eq. 5.2 more in line with the 2022 SENECT data. The frequency of the smaller diameters around 1 mm dominates for the combined method with a symmetric distribution in the 0.23 m s^{-1} range and a right skew.

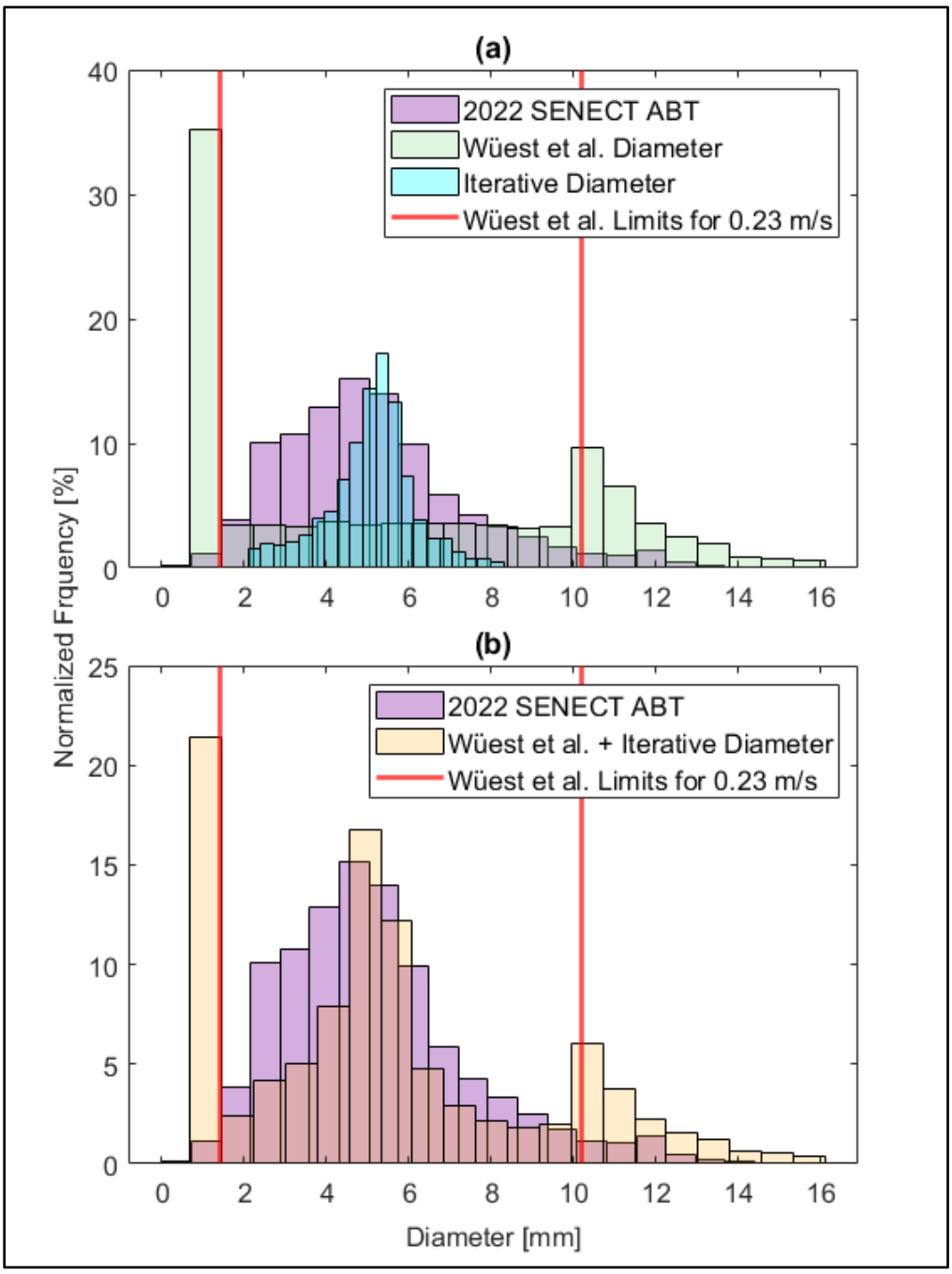

Figure 8. Bubble size distribution normalized by percentages. Figure 3 data were added for comparison as the purple histogram in both figures. (a) Green histogram shows Wüest et al. approximated diameters [1], and the force balance iterative method diameters is the cyan histogram. (b) Combining both methods resulted in the orange histogram. The red, vertical lines represent the diameter range edges for rising velocity 0.23 m s^{-1} in accordance with Wüest et al. [1].

4.3 BUBBLE RELEASE TIME AND LOCATION

To determine how active Cubillas Reservoir is in terms of ebullition, the data were processed to find binary data for bubble releases. If a bubble track is detected, it is registered as a bubble event occurring (refer to Section 3.3). A spatial and temporal analysis was performed since the deployment is stationary over the entire month and records data throughout the entire 24-hour day. Figure 9a and Figure 9b are the spatial data for all the released bubbles for the entire month, however, they are colored differently. The distribution over the area is relatively uniform with a dense cluster in the top left quadrant. The colors of each point in Figure 9a correspond to the hour of the day in Figure 9c, which also shows a uniform distribution. Figure 9c is the entirety of the month's bubble-released data binned into hours of the day. The 15^{th} hour, 15:00, was the most active. There is a bimodal distribution with more favoritism in the afternoon hours. The colors of Figure 9b correspond with the date in Figure 9d, there is a clear cluster of one color, which explains that there were days when that spot was more active, signaling a large bubbling event. Figure 9d is the entirety of the month's data binned by date. It is important to note that October 4^{th} and 5^{th} are underestimated in Figure 9d due to only having half the days' worth of collected data.

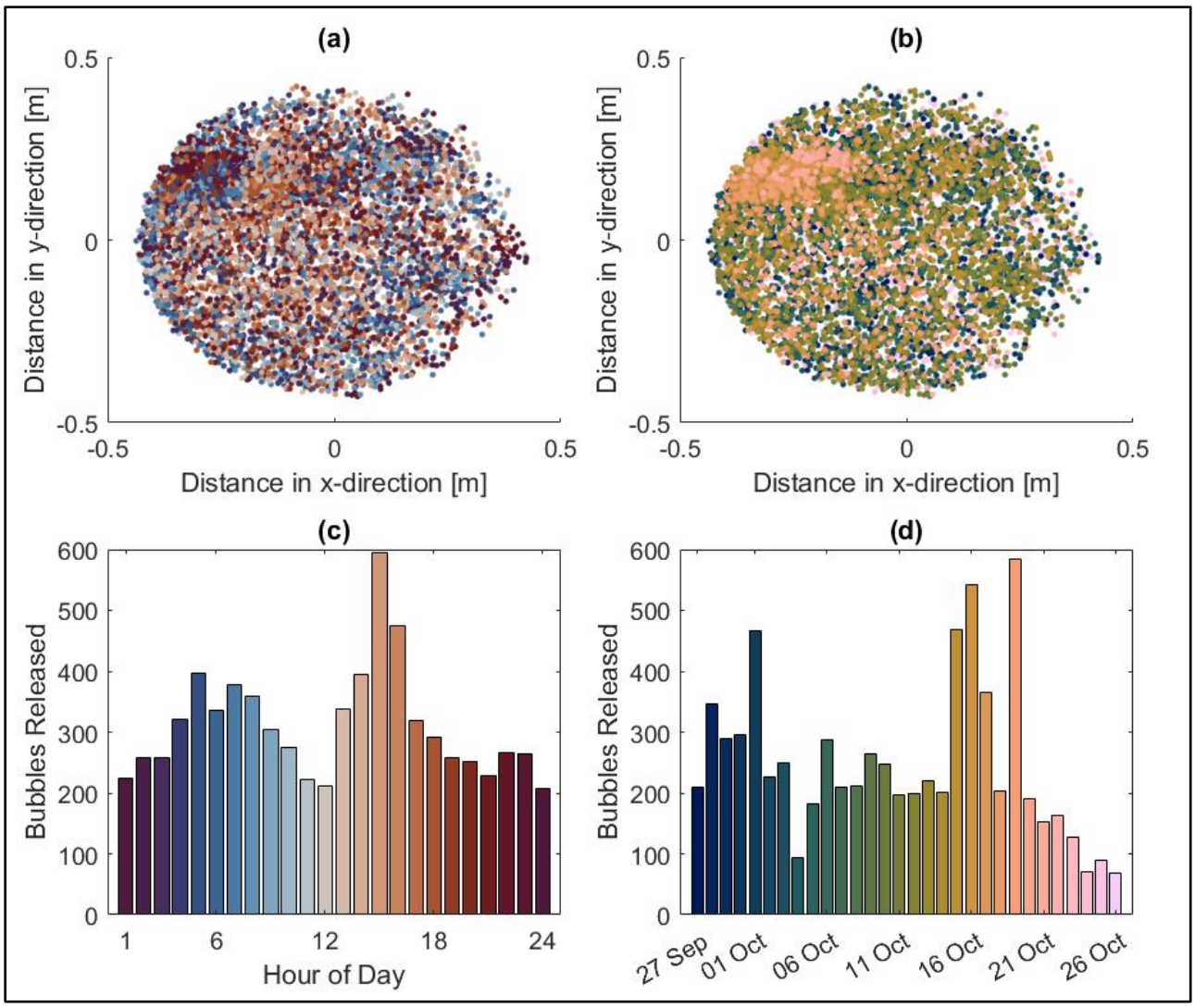

Figure 9. (a) Release of a single bubble in the 0.61 m^2 footprint of the transducer with color variation by hour of day. (b) Release of a single bubble in the 0.61 m^2 footprint of the transducer with color variation corresponding with day of year. (c) The entire month's released bubbles grouped by hour. (d) The entire month's released bubbles grouped by day.

To determine spatial variability of bubble release in greater depth, Figure 9a and Figure 9b are dissected to show any patterns. Figure 10 dissects Figure 9a. Figure 10 shows the top left quadrant of the footprint being more active than anywhere else. When more active hours approach (15^{th} and 16^{th} hour), the spatial variability is more evenly distributed across the footprint. Figure 11 is the dissection of Figure 9b. From Figure 11 there is a decline in bubbling events as the month progresses apart from October 15^{th} – 17^{th} and the 19^{th}. After October 19^{th}, the top left quadrant of

the footprint is particularly active for the rest of the deployment with sparse events everywhere else, which matches patterns of September 28th, October 13th, and October 14th. The left side of the footprint in general is more active than the right side.

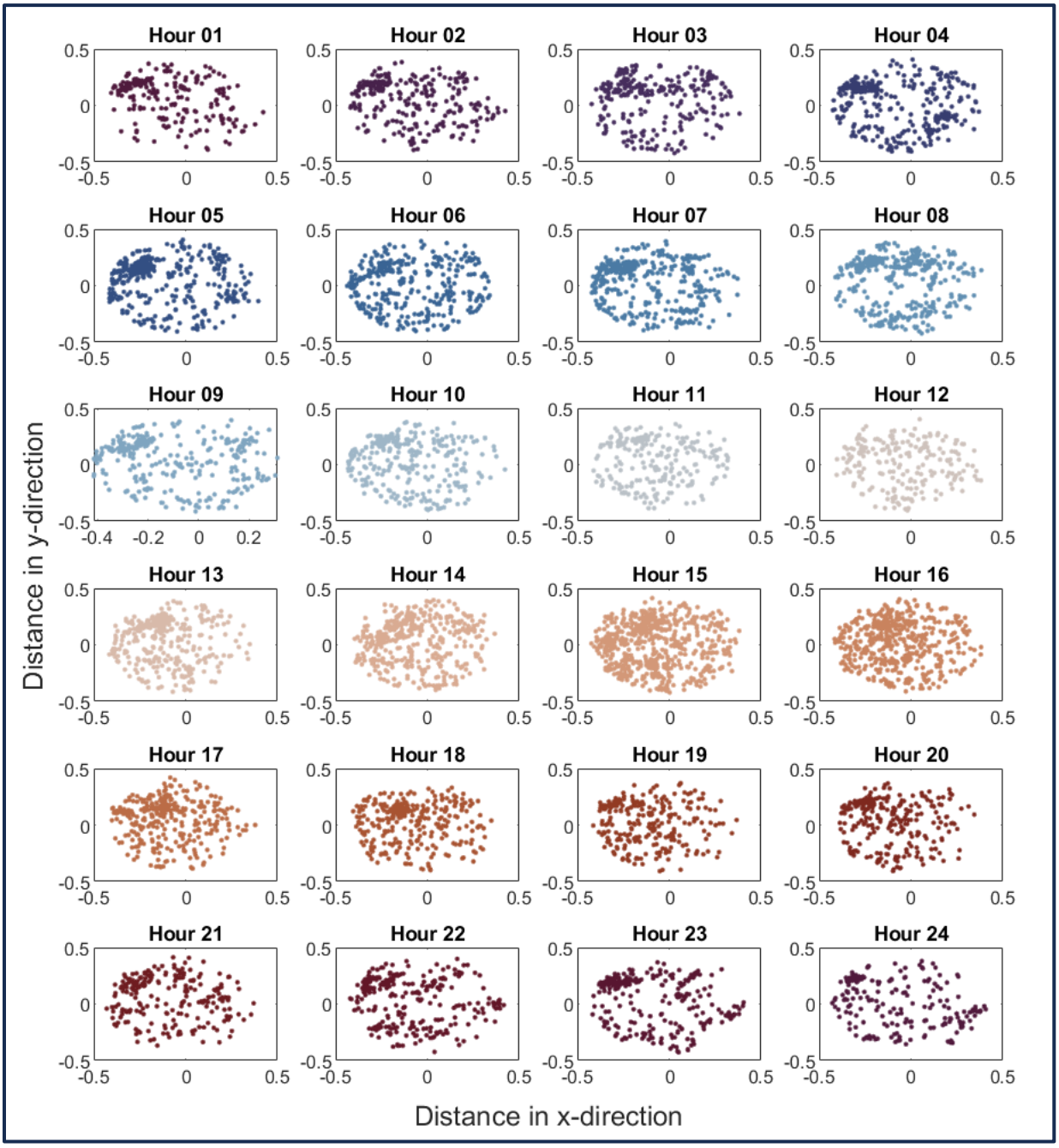

Figure 10. Spatial distribution of bubble releases in the transducer's footprint by hour over the entire month.

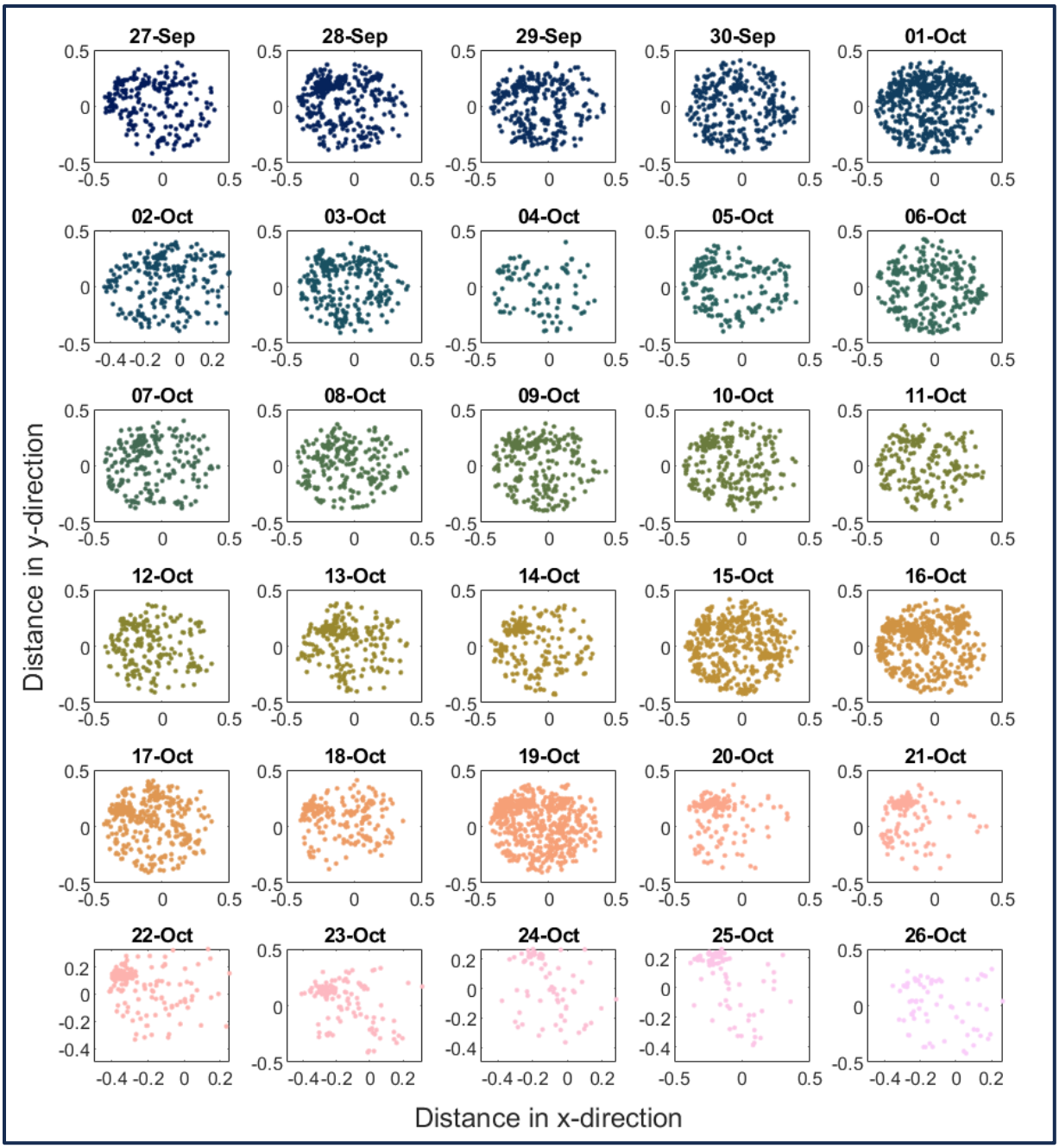

Figure 11. Spatial distribution of bubble releases in the transducer's footprint by day.

4.4 EBULLITION RATES

Using the two methods (Wüest et al. [1] and iterative force balance) to find diameter, the two datasets from Figure 8 were calculated in units of milliliters of air per unit area per time. This was done by summing bubble volumes over a specific period. Figure 12a shows the hourly ebullition

rates for the entire deployment using the two BioSonics methods and directly compares them to the measured ebullition rates found using the ABT. Using the iterative force balance method to determine bubble sizes, the rate was not at the same magnitude as the Wüest et al. approximation rate [1] and the ABT data. Using the calculated diameters from the combined method in Figure 8b, Figure 12b is produced. While both Figure 12a and Figure 12b look similar when comparing the Wüest et al. approximation [1] to the combined approximation, the results are different. To show the difference, Figure 13 is the same data from Figure 12 bin averaged by six-hour increments. The binned data shows that the relative magnitudes have similar trends (valleys and peaks) at the same times. The iterative force balance method was eliminated from Figure 13a since its hourly data was not near the same magnitude as the Wüest et al. approximation [1] or the ABT data in Figure 12a. Figure 13a shows the Wüest et al. approximation [1] to have similar trends and magnitudes to the ABT data. Figure 13b shows the combined method (Wüest et al. [1] with the iterative force balance) slightly underestimates ebullition gas flux rates when compared to the ABT data. Although Figure 8 shows a better size match between the 2022 SENECT data and the combined method, the Wüest et al. approximation [1] alone shows a better ebullition gas flux rate match to the concurrent ABT data in Figure 13. However, the combined method in Figure 12b is a decent approximation when compared to the ABT data on an hourly basis, especially towards the end of the deployment period.

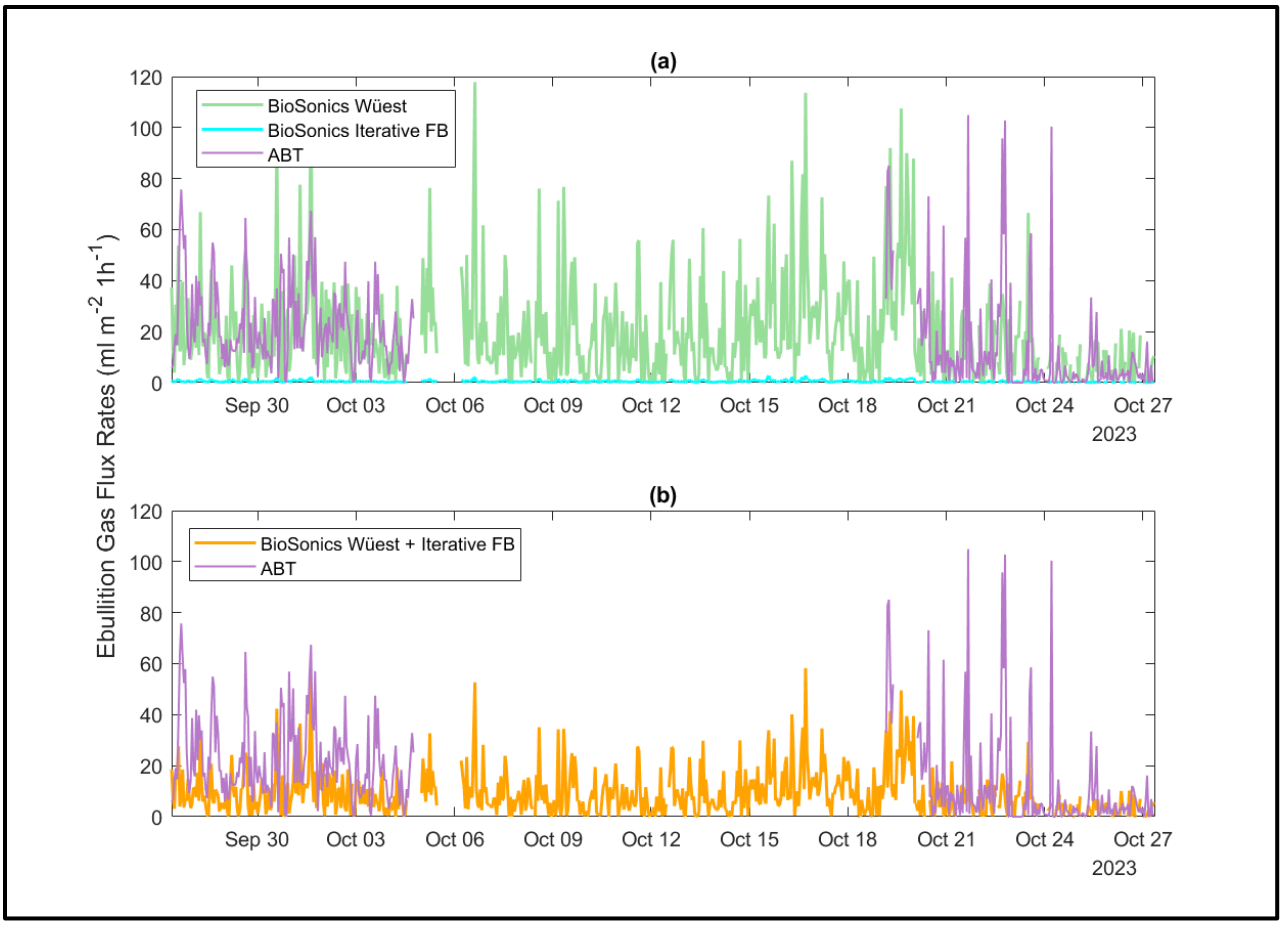

Figure 12. Hourly ebullition gas flux rates over the entire deployment using (a) the two BioSonics methods and ABT data. and (b) the combined Wüest et al. approximation [1] and the iterative force balance with the ABT data.

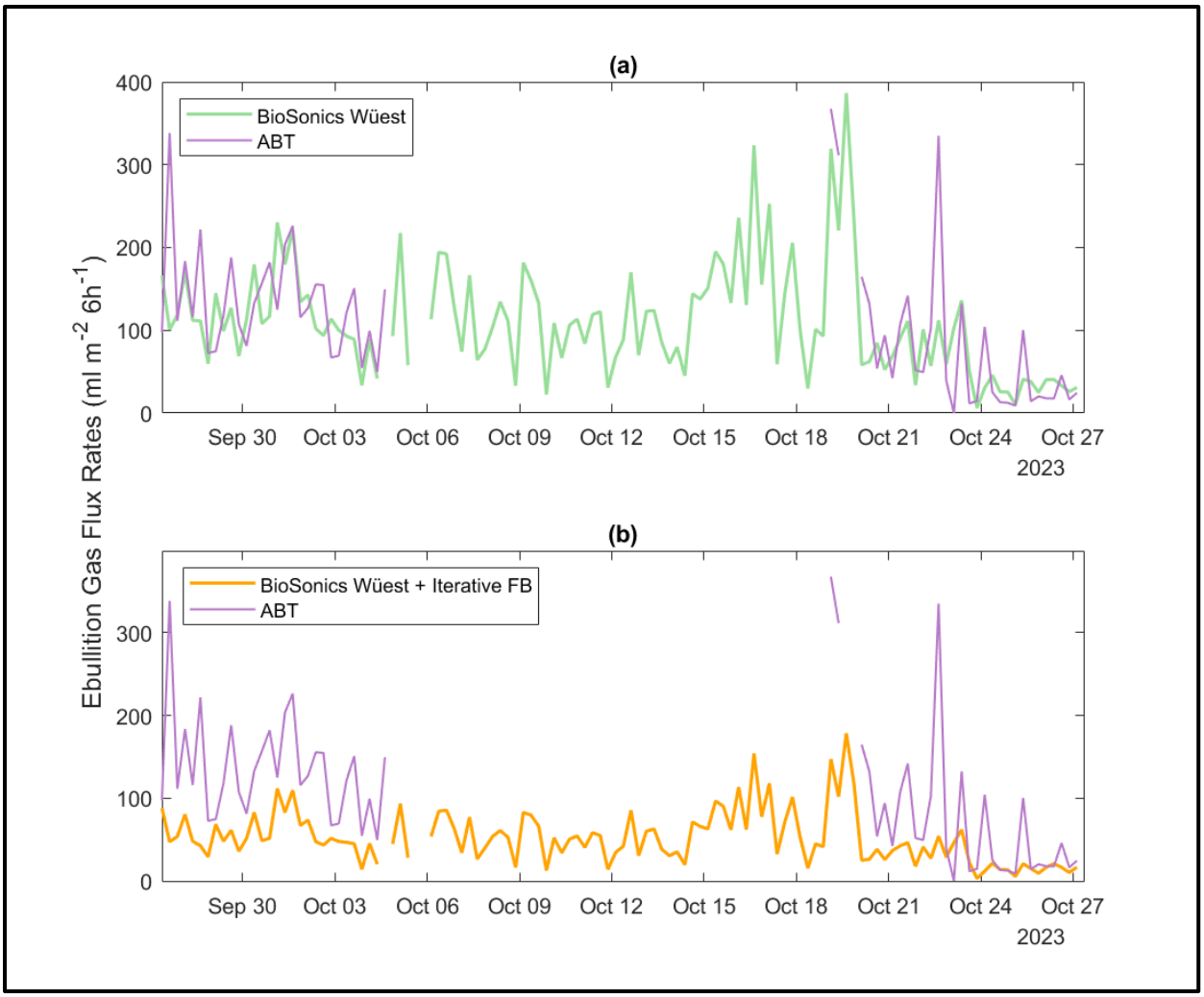

Figure 13. Ebullition gas flux rates bin averaged by six-hour increments over the entire deployment using (a) the Wüest et al. approximation [1] and ABT data and (b) the combined Wüest et al. approximation [1] and the iterative force balance with the ABT data.

5 DISCUSSION

5.1 BUBBLING LOCATION AND TIME

Cubillas Reservoir is an extremely active reservoir in terms of ebullition. Figure 9a shows an overall busy spatial plot of the transducer footprint except for a small area in the upper left, where a blue patch is clearly separated from a red patch. This was then dissected to find any true spatial variance (Figure 10). It was found that early hours had dense spots in the top left, whereas the afternoon hours, specifically 17:00 and 18:00, had dense clusters more towards the center left. The dissection in Figure 10 confirms the very slight separation of the morning and afternoon spatial variance. Figure 9b shows that combining spatial and temporal data can reveal daily clusters. Figure 9b shows a bubble event that occurs in one relative spot (top left) and corresponds to specific days in Figure 11, October 20^{th} – 25^{th}. These bubble events are likely more bursts happening in one spot in shorter periods of time, similar to findings made by Shiba [27], which can explain the slight color separation in the same area of Figure 9a then dissected in Figure 10. Overall, Figure 9a, Figure 9b, Figure 10, and Figure 11 present the spatial variability of the entire transducer footprint, confirming the sporadic and active nature of Cubillas Reservoir. However, it is noticeable that the left edge of the footprint is more active than the right edge. There is not enough information to confidently say what is causing this top left cluster, but small variabilities such as organic content can influence the results [11].

Figure 9c shows that there is a pattern where the most ebullition occurs in the afternoon hours and has lower activity in the night with slight increases as the morning comes. Literature confirms that warmer water temperatures increase methane fluxes, so it is expected that the peak happens during the warmest time of the day [24]. However, the morning flux increase cannot be explained by the

temperature since Figure 4 and Figure 6 show the reservoir losing heat in the nighttime. Figure 4 shows that wind speeds peak in the afternoon, typically at 15:00, and shows that wind speeds dramatically pick up in the morning hours. This increase in morning winds and increase in morning bubbling events is in agreement with findings that short-term water level fluctuations, such as those caused by wind shear, increase release of methane from an increase in mechanical energy into the system [23]. The large afternoon ebullitive flux and relatively lower nighttime flux supports previous work on methane fluxes via ebullition [9], [22]. Comparing Figure 9d and Figure 11 with Figure 13, there are peaks occurring at the same points as expected. The sharp decrease recorded by the BioSonics on October 19th into the 20th correlates with a relatively sharp decrease in wind speed and the water level increasing after a precipitation event, which further validates that relatively calmer, deeper sites have lower ebullition [11], [23]. The windier days, as seen in Figure 4, on October 17th and 19th, have relatively lower daily average heat content in Figure 6 and have different magnitudes in bubble events seen in Figure 9d. It is likely that the 19th has a significantly larger ebullitive flux due to higher wind speeds than the 17th. Figure 4, Figure 6, and Figure 13 support the diel pattern seen in Figure 9c with larger fluxes occurring in the morning and afternoon hours compared to nighttime and is validated by previous studies showing temperature, light, and wind effects on methane release [9], [24]. Overall, there is a decrease in ebullition gas flux rates as the month progresses (a daily average decrease of ~620 mL $m^{-2}d^{-1}$ from the start of the deployment to the end), with some larger bubbling events occurring with different meteorological events as seen in Figure 4 and Figure 5, and Figure 13. The decrease in ebullition gas flux rates seen towards the end of the deployment following a decrease in air temperature, wind speeds, heat content, and a higher water level. Additionally, this is in agreement with seasonal variations found in previous studies [11], [12], [22]. However, a limitation to this study is that only

one month's worth of data was collected, so determining seasonable variability from this study alone is not possible.

5.2 Iterative Force Balance and Wüest et al. Approximation

The two methods to find bubble sizes produced two distinctive datasets. Figure 8a shows the differences between the two and compares them both to the SENECT bubble size data collected in 2022. While there are differences in the frequency occurrence of the diameters (Figure 8), they all produced data in the same relative range. The distribution in Figure 8 is within the found range by Maeck et al. [11]. The iterative force balance diameters have the shortest range. This proves to be an issue once it is equivalent to an ebullitive flux rate, severely underestimating the released volume when compared to the ABT data (Figure 12a). From the collected rising velocities in Figure 7, the highest frequency, normalized by percentage, occurs around 0.23 m s^{-1}. The Wüest et al. approximation [1] has a radius range ($7.0*10^{-4}$ m < r < $5.1*10^{-3}$ m) for rising velocities at 0.23 m s^{-1}, and as a result, the data are purely an estimation for collected velocities at 0.23 m s^{-1}. This large range of radii occurs due to the changing shape of the rising bubble (see Section 2.2). In Figure 8a and Figure 8b, the red, vertical lines represent that unknown range, and each set has a different distribution in the range. Since Visual Aquatic cannot resolve sizes of bubbles, just their vertical velocities, there must be an estimation for that range noted by the red lines in Figure 8. Data from the SENECT ABT in 2022 is trustworthy in its size resolution in this range due to its methods of automatically measuring bubble volumes via gas trapping and finding their radii. To create a more accurate approximation in terms of size distribution to the SENECT ABT, a combination of the Wüest et al. approximation [1] and the iterative force balance was created and produced the results in Figure 8b, Figure 12b, and Figure 13b. Since the data from the SENECT ABT were collected in 2022 and did not capture data during September or October 2022, it is more

reliable to compare the methods calculating ebullition gas flux rates to the ebullition gas flux rates from the deployment concurrent ABT data.

Cubillas Reservoir is known for having consistent and abundant ebullition. Looking at the ebullition gas flux rates, Figure 13b shows that the combined BioSonics hydroacoustic methods for finding sizes of the individual bubbles underestimates the bubbling when compared to the ABT data. The discrepancy between the two methods (BioSonics combined method and ABT) is likely due to the size underestimation from the iterative force balance method. These results show that the iterative force balance method is not resolved enough for approximating ebullitive flux rates. Resolving the drag coefficient from an initial diameter guess did not provide a robust enough range of diameters (Figure 8). However, the Wüest et al. approximation [1] alone estimates ebullition gas flux rates closer to the ABT data in Figure 13a. There are differences between the Wüest et al. approximation [1] and the ABT data, particularly on October 22nd, 2023. The ABT is not directly over the transducer footprint, indicating that the recorded gas is likely from a different release spot than the transducer footprint which can alter the results of the ABT data. It is not expected that the two datasets match each other exactly, but having similar magnitudes and trends is a sign of a good approximation. Figure 12 and Figure 13 show that both the BioSonics combined approximation and the Wüest et al. approximation alone [1] have results within the same magnitude of the ABT data, whereas the BioSonics using the iterative force balance alone cannot produce the same. Figure 13a shows that peaks and valleys are occurring at the same points in time for the two datasets. These trends seen in both datasets coupled with meteorological and reservoir data (hydrodynamic processes, heat content, and diel patterns) is indicative of a good estimation of ebullition gas flux rates produced by the hydroacoustic method.

The Wüest et al. method [1] alone provides an approximation of ebullitive gas flux rates that aligns more closely with the ABT data in Figure 13. However, when considering bubble sizes, Figure 8 shows that the combined method offers a better approximation to the SENECT ABT. Further investigation is required to understand the discrepancies between the ebullitive gas flux rate results (Figure 12 and Figure 13) and the bubble size distribution (Figure 8). For instance, understanding a bubble's trajectory and path is crucial for identifying the origins of the gas collected in the SENECT ABT. It is possible that bubbles released outside the sonar's detection volume are later collected in the ABT, leading to an underestimation by the BioSonics method. However, this does not explain the closer estimation provided by the Wüest et al. method [1]. It is also possible that the combined method underestimates the actual sizes of the bubbles. While Figure 8b shows a bubble distribution from the combined method that is more comparable to the SENECT ABT data, it is important to note that the data are not concurrent with this deployment.

The fish blocking the signal of the transducer is a limitation to this study and can also be a reason why the BioSonics data are sometimes lower than the ABT data in Figure 13a, especially in the afternoon hours when the fish are most active (refer to Figure 2). Fish interference can disrupt the return signal to the transducer, there is likely an underestimation from this (as seen at 12:00 in Figure 9c). Fish can also disrupt the path of a bubble, resulting in the bubble being pushed out of the transducer's detection volume. The Visual Aquatic analysis configurations chosen to detect SED tracks in the first meter above the sediment and the code that filtered the linearity and rising velocity of the track to meet the conditions stated in Section 3.3 combat any stray fish entering the footprint. Another limitation to this study is not having the full reservoir resolved with ebullition gas flux data, so understanding the spatial variability of the entire reservoir cannot be determined from this alone.

Using the combined approximation for hydroacoustic measurements with the BioSonics DT-X Extreme Echosounder, an acceptable estimate of ebullition gas flux rates can be found. This method would prove to be extremely successful in a space that is deeper than Cubillas to avoid large schools of fish interfering with the signal. For reservoirs with ebullitive activity, this method is a non-invasive way to collect valuable data. To further this research, applying the same method to transects can resolve spatial variation in the reservoir and contribute to the research of depth and inflows influencing methane release.

6 CONCLUSIONS

Methane is a known potent greenhouse gas capable of storing more heat per molecule than carbon dioxide, and it is a large driver of climate change. While many anthropogenic sources have been studied, ecological microbial sources have been looked over despite accounting for approximately 30% of atmospheric methane emissions. Reservoirs are important for water resource management but can be ecological microbial sources of methane under anoxic conditions. The buildup of organic matter and the presence of microbes induce methanogenesis, the process of breaking down organic matter and releasing methane as a result. Methane is typically released into the atmosphere from reservoirs via diffusion and ebullition. Typical methods for determining methane emission rates from reservoirs include sediment analyses, air-water interface gas chambers or eddy covariance, bubble counters, and hydroacoustic in-situ measurements (often dependent on specific configurations). Many studies focus on methods that measure diffusive fluxes and some even group ebullition into these fluxes (i.e., an estimate of a total flux) or discard them all together. The lack of ebullitive gas flux measurements is problematic as it often accounts for over 50% of total emissions, as found in a study covering 32 different reservoirs, leading to a severe underestimation of their true emission rates [9]. Developing and testing new methods is important because of how difficult ebullition is to study and quantify. Hydroacoustic instruments are a newer approach needing further exploration in quantifying ebullition. This method is accessible to users in possession of hydroacoustic instruments and can help contribute to refining the true contribution reservoirs have to global greenhouse emissions.

This thesis demonstrates that hydroacoustic measurements are effective for non-invasive monitoring of methane fluxes via ebullition in a Mediterranean climate reservoir. Cubillas

Reservoir is an ideal study site due to its visually active ebullition throughout the day (Figure 2 and Figure 12). The BioSonics DT-X Extreme Echosounder was mounted to a stationary platform to collect 24-hour data over the entire one-month deployment. This method does not rely on specific instrument configurations, such as sampling frequency, which can be useful to many who already have a BioSonics Echosounder or an echosounder that can resolve single echo detection (SED) tracks. With the echosounder and the Visual Aquatic software, a reliable method for determining bubble sizes from the deployment was developed using the Wüest et al. bubble size approximation [1] (refer to Figure A-1 in the Appendix) and an iterative force balance method (Section 3.3). The combination of the Wüest et al. approximation [1] and a force balance (Eq. 6.2) on a single bubble provided a distribution of estimated bubble diameters from known rising bubble velocities. However, this analysis showed an underestimation of ebullition gas flux when compared to the SENECT Automatic Bubble Trap (ABT) data. The ebullitive gas flux estimations using the Wüest et al. approximation [1] compared well with concurrent ABT data, showing magnitudes and trends that matched. Applying this method to datasets that contain rising bubble velocities, time, and collection site dimensions (e.g. transducer swept volume and footprint) can reveal the ebullition gas flux rates for a reservoir, further expanding the research on how reservoirs contribute to global greenhouse gas fluxes.

Additionally, the ebullition gas flux results from the hydroacoustic measurements agree with current literature in that meteorological events, hydrodynamic processes, diel patterns, and heat content can influence rates. This was seen with a correlation between high wind events and an increase in ebullition events. Fewer ebullition events occurred (i) in the nighttime and early morning, (ii) when water level increased, and (iii) during periods with cooler air temperatures. The SED tracks also revealed spatial and temporal variability within the transducer footprint. The top

left of the transducer footprint showed consistent bubble clusters occurring on both a 24-hour and a day-to-day analysis across the entire month-long deployment.

There were limitations to this study. Limitations include a short deployment time (September 26th to October 26th, 2023), incomplete concurrent SENECT Automatic Bubble Trap dataset, lack of spatial variability across the reservoir, fish interference in the echograms, and a lack of definitive size resolution at a rising velocity of 0.23 m s^{-1} in the Wüest et al. approximation (Figure A-1) [1]. A longer deployment time can resolve system seasonality changes and understand bubbling events better in relation to meteorological events. If the concurrent SENECT ABT data were complete for the full deployment period, analyzing the BioSonics method for measuring ebullition would be more definitive for the period. A better understanding of spatial variability across the reservoir requires having more stationary deployments to see if there are any changes in methane production across the reservoir. To prevent fish interference in the future, a cage or net can be placed around the deployment site to keep fish out of the sonar's detection area. This will help ensure that echograms are free from false bubble data caused by the presence of fish.

Despite these limitations, this thesis presents a promising approach to measure ebullitive gas flux rates in reservoirs. The results provide a good approximation for this reservoir system compared to automatic bubble trap data. This method can be applied to transects as future work in this or other systems to determine the spatial variability in ebullitive fluxes that the system may have.

Future research could improve upon this method by considering the limitations stated to achieve more definitive conclusions. This method provides a new approach to quantifying ebullition gas fluxes from reservoirs using recorded SED tracks provided by hydroacoustic measurements. Reservoirs in similar climatic conditions are underestimated globally with respect to their CH_4 fluxes, which makes this area of research important to expand on. Reservoirs play a key role in

water resource engineering and provide many important functions to society, but the global greenhouse gas emissions released from them are an unintended product. Understanding reservoir systems better is vital to making decisions that impact both water resources and GHG emissions.

7 REFERENCES

[1] A. Wüest, N. H. Brooks, and D. M. Imboden, "Bubble plume modeling for lake restoration," *Water Resour. Res.*, vol. 28, no. 12, pp. 3235–3250, Dec. 1992, doi: 10.1029/92WR01681.

[2] "Methane." [Online]. Available: https://climate.nasa.gov/vital-signs/methane/?intent=121

[3] "What makes methane a more potent greenhouse gas than carbon dioxide?," MIT Climate Portal. [Online]. Available: https://climate.mit.edu/ask-mit/what-makes-methane-more-potent-greenhouse-gas-carbon-dioxide

[4] "Overview of Greenhouse Gases," EPA. [Online]. Available: https://www.epa.gov/ghgemissions/overview-greenhouse-gases

[5] Y. Oh *et al.*, "CarbonTracker CH4 2023," 2023, *NOAA Global Monitoring Laboratory*. doi: 10.25925/40JT-QD67.

[6] K. Thoning, E. Dlugokencky, X. Lan, and NOAA Global Monitoring Laboratory, "Trends in globally-averaged CH4, N2O, and SF6." NOAA GML, 2022. doi: 10.15138/P8XG-AA10.

[7] R. B. Jackson *et al.*, "Atmospheric methane removal: a research agenda," *Philos. Trans. R. Soc. Math. Phys. Eng. Sci.*, vol. 379, no. 2210, p. 20200454, Nov. 2021, doi: 10.1098/rsta.2020.0454.

[8] K. Calvin *et al.*, "IPCC, 2023: Climate Change 2023: Synthesis Report. Contribution of Working Groups I, II and III to the Sixth Assessment Report of the Intergovernmental Panel on Climate Change [Core Writing Team, H. Lee and J. Romero (eds.)]. IPCC, Geneva, Switzerland.," Intergovernmental Panel on Climate Change (IPCC), Jul. 2023. doi: 10.59327/IPCC/AR6-9789291691647.

[9] J. J. Beaulieu *et al.*, "Methane and Carbon Dioxide Emissions From Reservoirs: Controls and Upscaling," *J. Geophys. Res. Biogeosciences*, vol. 125, no. 12, p. e2019JG005474, Dec. 2020, doi: 10.1029/2019JG005474.

[10] J. A. Harrison, Y. T. Prairie, S. Mercier-Blais, and C. Soued, "Year-2020 Global Distribution and Pathways of Reservoir Methane and Carbon Dioxide Emissions According to the Greenhouse Gas From Reservoirs (G-res) Model," *Glob. Biogeochem. Cycles*, vol. 35, no. 6, p. e2020GB006888, Jun. 2021, doi: 10.1029/2020GB006888.

[11] A. Maeck *et al.*, "Sediment Trapping by Dams Creates Methane Emission Hot Spots," *Environ. Sci. Technol.*, vol. 47, no. 15, pp. 8130–8137, Aug. 2013, doi: 10.1021/es4003907.

[12] D. Martinez and M. A. Anderson, "Methane production and ebullition in a shallow, artificially aerated, eutrophic temperate lake (Lake Elsinore, CA)," *Sci. Total Environ.*, vol. 454–455, pp. 457–465, Jun. 2013, doi: 10.1016/j.scitotenv.2013.03.040.

[13] "5.9D: Methanogenesis," LibreTexts: Biology. [Online]. Available: https://bio.libretexts.org/Bookshelves/Microbiology/Microbiology_(Boundless)/05%3A_Microbial_Metabolism/5.09%3A_Anaerobic_Respiration/5.9D%3A_Methanogenesis

[14] G. Schäfer, "Membrane-Associated Energy Transduction in Bacteria and Archaea," in *Encyclopedia of Biological Chemistry*, Elsevier, 2013, pp. 28–35. doi: 10.1016/B978-0-12-378630-2.00207-3.

[15] D. Bastviken, L. J. Tranvik, J. A. Downing, P. M. Crill, and A. Enrich-Prast, "Freshwater Methane Emissions Offset the Continental Carbon Sink," *Science*, vol. 331, no. 6013, pp. 50–50, Jan. 2011, doi: 10.1126/science.1196808.

[16] I. Ostrovsky, D. F. McGinnis, L. Lapidus, and W. Eckert, "Quantifying gas ebullition with echosounder: the role of methane transport by bubbles in a medium-sized lake: Measuring

methane transport with bubbles," *Limnol. Oceanogr. Methods*, vol. 6, no. 2, pp. 105–118, Feb. 2008, doi: 10.4319/lom.2008.6.105.

[17] B. R. Deemer *et al.*, "Greenhouse Gas Emissions from Reservoir Water Surfaces: A New Global Synthesis," *BioScience*, vol. 66, no. 11, pp. 949–964, Nov. 2016, doi: 10.1093/biosci/biw117.

[18] T. DelSontro, L. Boutet, A. St-Pierre, P. A. Del Giorgio, and Y. T. Prairie, "Methane ebullition and diffusion from northern ponds and lakes regulated by the interaction between temperature and system productivity," *Limnol. Oceanogr.*, vol. 61, no. S1, Nov. 2016, doi: 10.1002/lno.10335.

[19] "Osmosis and Diffusion." [Online]. Available: https://chem.libretexts.org/@go/page/155680

[20] D. Bastviken, J. J. Cole, M. L. Pace, and M. C. Van De Bogert, "Fates of methane from different lake habitats: Connecting whole-lake budgets and CH $_4$ emissions," *J. Geophys. Res. Biogeosciences*, vol. 113, no. G2, p. 2007JG000608, Jun. 2008, doi: 10.1029/2007JG000608.

[21] B. P. Scandella, C. Varadharajan, H. F. Hemond, C. Ruppel, and R. Juanes, "A conduit dilation model of methane venting from lake sediments: METHANE VENTING FROM LAKE SEDIMENTS," *Geophys. Res. Lett.*, vol. 38, no. 6, p. n/a-n/a, Mar. 2011, doi: 10.1029/2011GL046768.

[22] M. Tušer, T. Picek, Z. Sajdlová, T. Jůza, M. Muška, and J. Frouzová, "Seasonal and Spatial Dynamics of Gas Ebullition in a Temperate Water-Storage Reservoir," *Water Resour. Res.*, vol. 53, no. 10, pp. 8266–8276, Oct. 2017, doi: 10.1002/2017WR020694.

[23] H. Hofmann, A. Lorke, and F. Peeters, "Temporal scales of water-level fluctuations in lakes and their ecological implications," *Hydrobiologia*, vol. 613, no. 1, pp. 85–96, Nov. 2008, doi: 10.1007/s10750-008-9474-1.

[24] A. K. Sieczko *et al.*, "Diel variability of methane emissions from lakes," *Proc. Natl. Acad. Sci.*, vol. 117, no. 35, pp. 21488–21494, Sep. 2020, doi: 10.1073/pnas.2006024117.

[25] M. A. Anderson and P. Pacheco, "Characterization of bottom sediments in lakes using hydroacoustic methods and comparison with laboratory measurements," *Water Res.*, vol. 45, no. 15, pp. 4399–4408, Oct. 2011, doi: 10.1016/j.watres.2011.05.029.

[26] T. DelSontro, M. J. Kunz, T. Kempter, A. Wüest, B. Wehrli, and D. B. Senn, "Spatial Heterogeneity of Methane Ebullition in a Large Tropical Reservoir," *Environ. Sci. Technol.*, vol. 45, no. 23, pp. 9866–9873, Dec. 2011, doi: 10.1021/es2005545.

[27] J. Shiba, "Mechanisms of Methane Release From Lake Sediments," University of California, Riverside, 2015.

[28] A. S. Salomatin, V. I. Yusupov, O. F. Vereshchagina, and D. V. Chernykh, "An acoustic estimate of methane concentration in a water column in regions of methane bubble release," *Acoust. Phys.*, vol. 60, no. 6, pp. 671–677, Nov. 2014, doi: 10.1134/S1063771014050133.

[29] W. L. Haberman and R. K. Morton, "An Experimental Study of Bubbles Moving in Liquids," *Trans. Am. Soc. Civ. Eng.*, vol. 121, pp. 227–250, 1956.

[30] W. L. Haberman, R. K. Morton, and D. W. T. M. Basin, *AN EXPERIMENTAL INVESTIGATION OF THE DRAG AND SHAPE OF AIR BUBBLES RISING IN VARIOUS LIQUIDS*. Washington, D.C, Navy Dept., David W. Taylor Model Basin, 1953.

[31] Benjamin. Rosenberg and D. W. T. M. Basin, *The Drag and shape of air bubbles moving in liquids*. Washington, D.C, Navy Dept., David W. Taylor Model Basin, 1950. [Online]. Available: https://www.biodiversitylibrary.org/item/102405

[32] N. M. Aybers and A. Tapucu, “Studies on the drag and shape of gas bubbles rising through a stagnant liquid,” *Wärme- Stoffübertrag.*, vol. 2, no. 3, pp. 171–177, Sep. 1969, doi: 10.1007/BF00751164.
[33] D. G. Karamanev and L. N. Nikolov, “Free rising spheres do not obey newton’s law for free settling,” *AIChE J.*, vol. 38, no. 11, pp. 1843–1846, Nov. 1992, doi: 10.1002/aic.690381116.
[34] X. Yan, Y. Jia, L. Wang, and Y. Cao, “Drag coefficient fluctuation prediction of a single bubble rising in water,” *Chem. Eng. J.*, vol. 316, pp. 553–562, May 2017, doi: 10.1016/j.cej.2017.01.137.
[35] “Eötvös Number,” Wolfram. [Online]. Available: https://resources.wolframcloud.com/FormulaRepository/resources/Etvs-Number
[36] A. Frohn and N. Roth, *Dynamics of droplets*. in Experimental fluid mechanics. Berlin Heidelberg New York Barcelona Hong Kong London Milano Paris Singapore Tokyo: Springer, 2000.
[37] R. Manica, E. Klaseboer, and D. Y. C. Chan, “Force Balance Model for Bubble Rise, Impact, and Bounce from Solid Surfaces,” *Langmuir*, vol. 31, no. 24, pp. 6763–6772, Jun. 2015, doi: 10.1021/acs.langmuir.5b01451.
[38] S. H. Park, C. Park, J. Lee, and B. Lee, “A Simple Parameterization for the Rising Velocity of Bubbles in a Liquid Pool,” *Nucl. Eng. Technol.*, vol. 49, no. 4, pp. 692–699, Jun. 2017, doi: 10.1016/j.net.2016.12.006.
[39] “Water Dams in Granada,” Andalucia Rustica. [Online]. Available: https://andaluciarustica.com/en/cubillas-dam.htm
[40] “Chapter 1, The Decomposition Process,” Texas A&M AgriLife. [Online]. Available: https://aggie-horticulture.tamu.edu/earthkind/landscape/dont-bag-it/chapter-1-the-decomposition-process/#:~:text=Intensive%20reduction%20of%20organic%20matter,sulfur%2Dcontaining%20organic%20compound).
[41] “DT-X Extreme Autonomous Portable Scientific Echosounder User Guide.” BioSonics, Inc.
[42] G. Boyra, G. Moreno, B. Orue, B. Sobradillo, and I. Sancristobal, “In situ target strength of bigeye tuna (Thunnus obesus) associated with fish aggregating devices,” *ICES J. Mar. Sci.*, p. fsz131, Jul. 2019, doi: 10.1093/icesjms/fsz131.
[43] D. M. Livingstone and D. M. Imboden, “Annual heat balance and equilibrium temperature of Lake Aegeri, Switzerland,” *Aquat. Sci.*, vol. 51, no. 4, pp. 351–369, 1989, doi: 10.1007/BF00877177.
[44] “Net Radiation,” NASA Earth Observatory. [Online]. Available: https://earthobservatory.nasa.gov/global-maps/CERES_NETFLUX_M

8 APPENDIX

8.1 ITERATIVE FORCE BALANCE EXAMPLE MATLAB CODE

```
for i = 1:length(dum3)

    d0 = 0.00029; % initial diameter guess [m]
    if error > 0.000001
        Re = zvel(dum3(i))*d0/nu;
            if Re > 1000
                Cd(i) = 0.44; % Eq. 3.2
            elseif Re <= 1000
                Cd(i) = 24*(1+0.15*Re.^0.687)/Re; % Eq. 3.1
            end
        d1 = 0.75*zvel(dum3(i))^2*Cd(i)/g; % Eq. 6.2
        error = abs(d1-d0);
        d0 = d1;
    end

    Rbubble(dum3(i)) = d1/2; % Radius
end
```

8.2 FIGURES

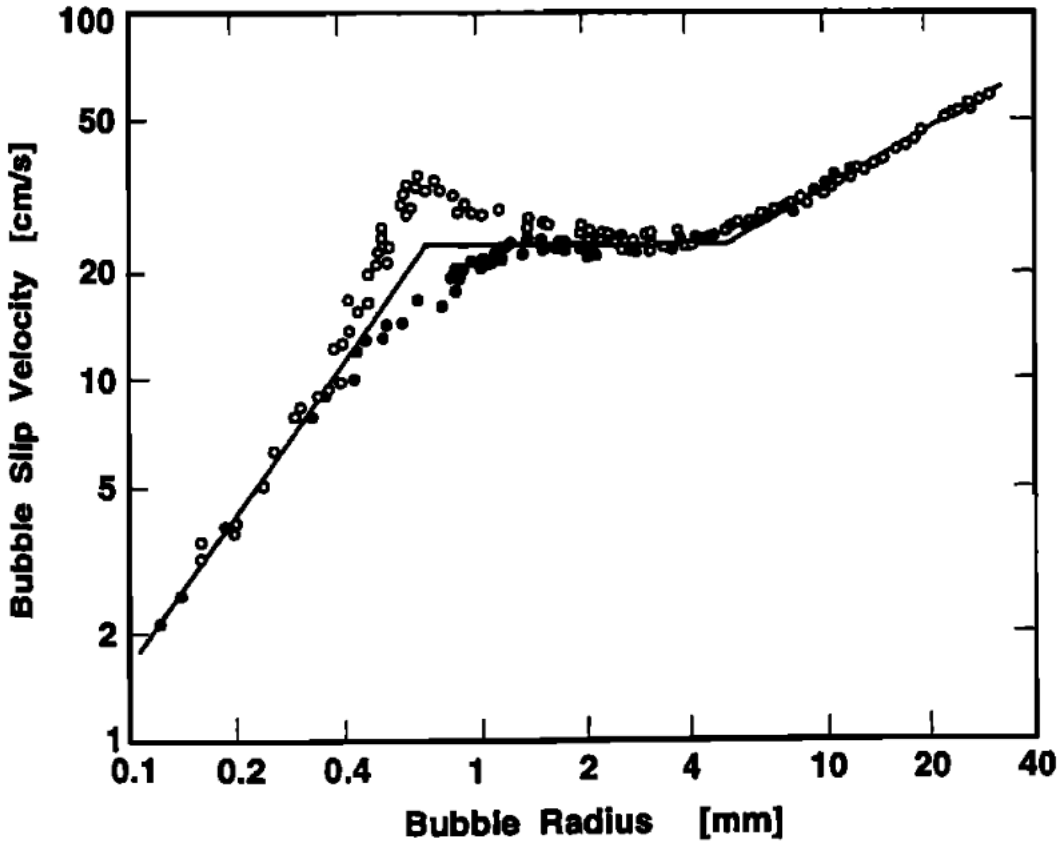

Figure A- 1. Wüest et al. Figure 5 [1] Terminal slip velocity versus bubble radius as found by closed data points (tap water) and open data points (distilled water) by Haberman and Morton [29].